LASER & PHOTONICS REVIEWS

www.lpr-journal.org

Maxwell Meets Marangoni—A Review of Theories on Laser-Induced Periodic Surface Structures

Jörn Bonse and Stephan Gräf*

Surface nanostructuring enables the manipulation of many essential surface properties. With the recent rapid advancements in laser technology, a contactless large-area processing at rates of up to $m^2\ s^{-1}$ becomes feasible that allows new industrial applications in medicine, optics, tribology, biology, etc. On the other hand, the last two decades enable extremely successful and intense research in the field of so-called laser-induced periodic surface structures (LIPSS, ripples). Different types of these structures featuring periods of hundreds of nanometers only—far beyond the optical diffraction limit—up to several micrometers are easily manufactured in a single-step process and can be widely controlled by a proper choice of the laser processing conditions. From a theoretical point of view, however, a vivid and very controversial debate emerges, whether LIPSS originate from electromagnetic effects or are caused by matter reorganization. This article aims to close a gap in the available literature on LIPSS by reviewing the currently existent theories of LIPSS along with their numerical implementations and by providing a comparison and critical assessment of these approaches.

1. Introduction

Laser-induced periodic surface structures (LIPSS) are a phenomenon whose discovery dates back to the time when the first laser sources were developed.[1] Nowadays, it is well established that LIPSS can be fabricated on almost all types of materials (metals, semiconductors, dielectrics). They are generated within the focal spot of the linearly polarized laser radiation and can be characterized as a periodic modulation of the surface topography in the form of a regular grating. Based on their spatial period Λ in relation to the utilized laser wavelength λ, LIPSS are divided into two groups: Low-spatial frequency LIPSS (LSFL) with $\Lambda > \lambda/2$ and high-spatial frequency LIPSS (HSFL) with $\Lambda < \lambda/2$. A sub-classification of the LSFL is based on the period of the structures and their orientation relative to the beam polarization direction, which are both determined by the electronic structure of the material and thus by the laser–matter interaction. While on strong absorbing materials, such as metals and semiconductors, LSFL are mainly characterized by $\Lambda \sim \lambda$ and an orientation perpendicular to the beam polarization (LSFL-I, see **Figure 1**a), on some large bandgap materials, such as fused silica, LIPSS are generated with $\Lambda \sim \lambda/n$ parallel to the beam polarization (LSFL-II, see Figure 1c). Here, n refers to the refractive index of the respective dielectric material.

With the first observation of the filigree HSFL during the 1990s with a spatial period of a few hundreds of nanometers only,[2] research activities in the field of LIPSS-based surface nanostructuring have increased significantly. The rapidly growing interest was triggered on the one hand by the availability and reliability of ultrashort pulse lasers, as the HSFL are predominately observed for laser pulse durations in the fs- to ps-range. On the other hand, another important reason is related to the periodicities of this "non-classical" type of LIPSS, which are significantly smaller than λ and thus allow laser-based nanostructuring far below the optical diffraction limit. According to the depth-to-period aspect ratio A, HSFL are classified into the types HSFL-I, with $A > 1$ (Figure 1d), and HSFL-II, with $A < 1$ (Figure 1b), respectively.

There are numerous experimental studies that systematically investigated the formation process of the above-mentioned types of LIPSS on different materials as a function of various laser and process parameters.[5–7] In recent years, the focus of experimental research has increasingly shifted toward the application of the gained knowledge aiming on the generation of tailored LIPSS for the creation of functional surface properties.[8–14] From the beginning, the experimental work was accompanied by theoretical studies on LIPSS formation, which is why today a large variety of model approaches is available that discuss the origin of LIPSS from sometimes very different perspectives. The objective of the present review article is to provide a systematic and comprehensive overview of the available LIPSS theories along with their historical context (Section 2), starting from the very first "simple"

Dr. J. Bonse
Bundesanstalt für Materialforschung und -prüfung (BAM)
Unter den Eichen 87
Berlin D-12205, Germany
E-mail: joern.bonse@bam.de
Dr. S. Gräf
Otto-Schott-Institut für Materialforschung (OSIM)
Friedrich-Schiller-Universität Jena
Löbdergraben 32
Jena D-07743, Germany

The ORCID identification number(s) for the author(s) of this article can be found under https://doi.org/10.1002/lpor.202000215

DOI: 10.1002/lpor.202000215

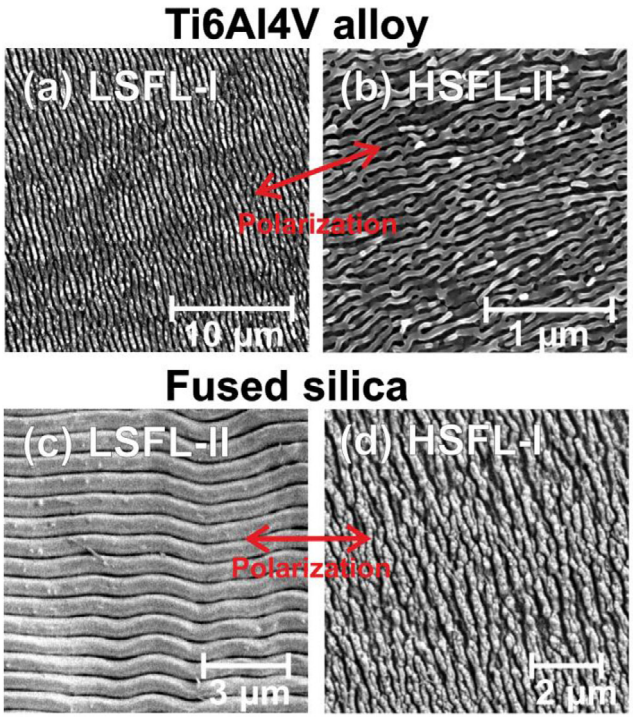

Figure 1. Examples of SEM images of different types of LIPSS (LSFL, HSFL) generated with different fs-laser irradiation conditions on metallic Ti6Al4V titanium alloy (upper row) and on dielectric fused silica (lower row). a) LSFL-I on Ti6Al4V [$\lambda = 790$ nm, $\phi_0 = 0.11$ J cm^{-2}, $N_{\text{eff,1D}} = 56$, 30 fs, 1 kHz, one pass]; b) HSFL-II on Ti6Al4V [$\lambda = 790$ nm, $\phi_0 = 0.08$ J cm^{-2}, $N_{\text{eff,1D}} = 280$, 30 fs, 1 kHz, two passes]; c) LSFL-II on fused silica [$\lambda = 800$ nm, $\phi_0 = 3.9$ J cm^{-2}, $N = 100$, 50 fs, 0.25 kHz]; d) HSFL-I on fused silica [$\lambda = 1025$ nm, $\phi_0 = 4.5$ J cm^{-2}, $N_{\text{eff,2D}} = 63$, 300 fs, 100 kHz, one pass]. The red double-arrows indicate the direction of the linear laser beam polarization. Note the different magnifications of the top-view SEM micrographs. (a,b) Reproduced with permission.[3] Copyright 2015, J. Bonse et al., published by De Gruyter. (c) Reproduced with permission.[4] Copyright 2013, AIP Publishing.

interference models to the current state of the art (Section 3). This also includes a wide range of numerical methods that are used as versatile tools for solving the underlying mathematical equations. As a concluding point, in Section 4 the reader is given a critical evaluation of the available LIPSS theories and numerical methods with regard to their weaknesses, common mistakes found in literature, and a comparison of their capabilities and performances.

2. Historic Developments

LIPSS were reported first in 1965 by Birnbaum on polished germanium crystal surfaces irradiated with a focused ruby laser beam.[1] He attributed the phenomenon to diffraction effects and proposed that the surface relief is formed by localized material removal at the maxima of the intensity pattern.

During the following more than five decades, the topic LIPSS has evolved into a scientific evergreen.[15] While the early experimental observation of LIPSS has triggered a continuously evolving research interest, the groundbreaking studies performed independently during the eighties of the twentieth century by two north American groups brought a remarkable understanding of the formation mechanisms of "classical" near-wavelength sized LIPSS (LSFL) for laser pulses with durations down to the nanosecond regime.[16–22] At that time, these studies left not too many questions open in the field. Hence, during the following decade much less research focused on LIPSS until new research interest was initiated by the observation of a new type of "non-classical" LIPSS with periods significantly smaller than the irradiation wavelength.[15]

Figure 2 visualizes in a timeline diagram the historic developments of different approaches for explaining laser-induced periodic surface structures, ordered by modeled physical phenomena and simulation techniques applied. These different theories will be explained and discussed in more detail in the following Section 3.

3. Theories of LIPSS

The currently existing theories on the formation of LIPSS can be divided in two different classes, i.e., i) electromagnetic theories describing the deposition of optical energy into the solid and ii) matter reorganization theories, which are based on the redistribution of surface near matter (**Figure 3**). One fundamental difference between both classes can be summarized as follows: while through electromagnetic scattering and absorption effects, the spatial signature of the final structures is already seeded during the laser irradiation, the reorganization of matter may take significantly longer (typically tens to hundreds of ps up to ms).

Hence, for the irradiation of solids by ultrashort laser pulses with durations in the fs to ps range, both formation scenarios occur in temporally separated regimes, which allows to experimentally distinguish between them through time-resolved experiments.[4,24–26] The following two sections provide a survey of existent electromagnetic LIPSS theories (Section 3.1) and of alternative models based on the reorganization of surface material (Section 3.2), both with a focus on the irradiation characteristics of ultrashort laser pulses and considering contributions with a detailed theoretical formalism only.

3.1. Electromagnetic Theories

Detailed electromagnetic theories on the formation of LIPSS, based on interference of electromagnetic radiation scattered at the microscopic rough surface, were developed during the eighties of the past century.[17,18,27] The basic idea behind these theories is sketched in **Figure 4**: During the laser irradiation the incident light scatters at the roughness of the sample surface (Figure 4a), e.g., via coherently driven elementary Huygens waves. For specific conditions, other surface excitation modes may be additionally excited such as surface plasmon polaritons (SPPs, see Figure 4b and for details the following Section 3.1.1). The

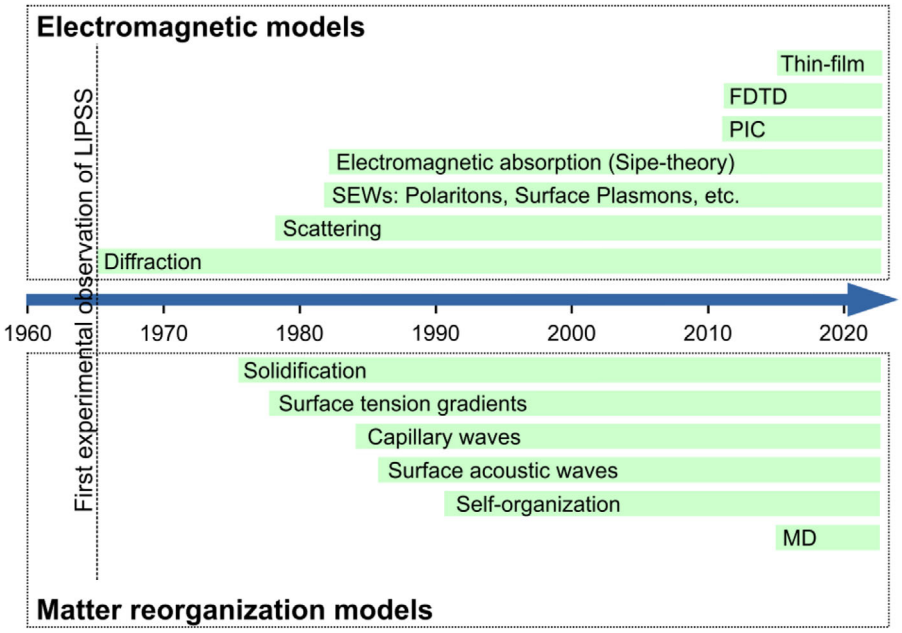

Figure 2. Historic timeline of the development of LIPSS theories based on electromagnetic approaches (top) or matter reorganization models (bottom).

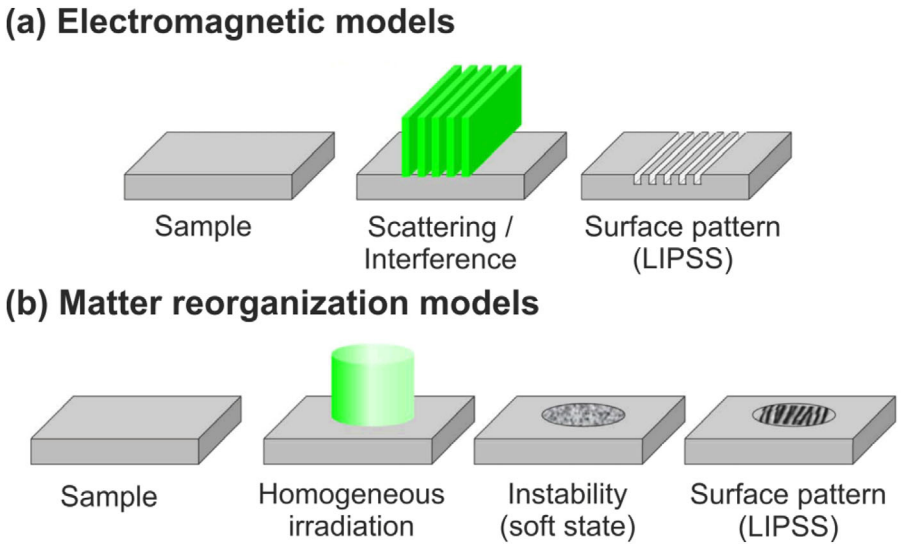

Figure 3. Fundamental processes occurring during LIPSS formation according to a) electromagnetic models and b) matter reorganization models. Adapted with permission.[23] Copyright 2013, Japan Laser Processing Society.

interference of the incident radiation with that emerging from scattering and SPPs leads to a spatial modulation of the local energy (fluence) distribution that—via absorption—is imprinted to the sample material (Figure 4c). For sufficiently strong laser excitation, the formation of the final periodic surface relief is then triggered, e.g., via spatially modulated material removal (ablation). Apart from the interference between the incident laser radiation and the electromagnetic field of the plasmons forming the primary LIPSS grating, additional second-order contributions may arise from the interference of (counter)propagating SPPs.[8]

3.1.1. Surface Electromagnetic Waves (SEWs) and SPPs

Some electromagnetic theories involve the excitation of different types of SEWs[28,29] including surface polaritons and specifically SPPs.[30] SPPs originate from delocalized coherent electron density oscillations and are bound to and propagate along the interface between two different media.[31] Driven by the external electromagnetic fields, they are localized in the vicinity of the interface and are damped out on both sides. SPPs exist in a coupled way in both media, and thus may have different characteristics than conventional free propagating electromagnetic waves.

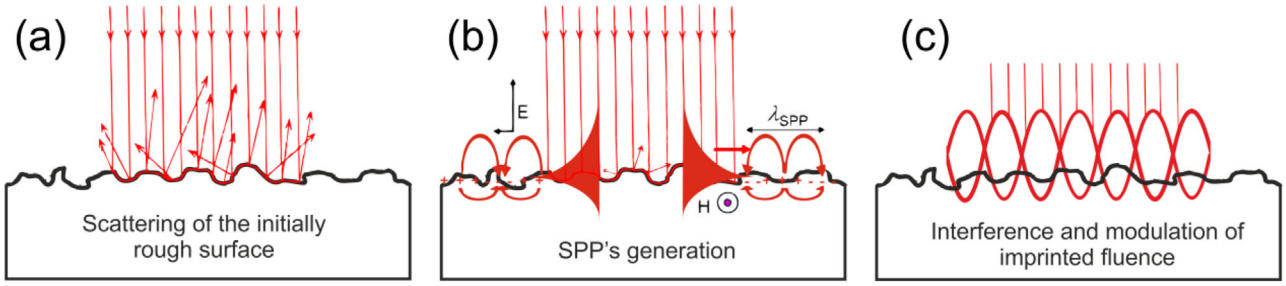

Figure 4. Scheme of electromagnetic formation mechanisms of LIPSS. The laser radiation (red) impacts the sample from the top. Its initial surface roughness results in a) optical scattering that may lead to the excitation of b) SPPs that interfere with the incident light and modulate the absorbed fluence pattern "imprinted" in the material. c) Finally, modulated ablation results in periodic surface structures. Reproduced with permission.[12] Copyright 2020, Laser Institute of America.

The corresponding theories are based on analytic mathematical equations. They often allow the prediction of LIPSS periods as function of specific irradiation parameters and material properties. However, they do not explicitly include feedback mechanisms describing pulse-to-pulse changes of the surface topography.

The most prominent (and simple) approach invokes the involvement of SPPs at the irradiated surface exposed to air/vacuum or another dielectric medium (e.g., a transparent liquid). For the excitation of SPPs, specific conditions on the dielectric permittivity of the two involved media have to be fulfilled.[32] For common metals (m) in contact with a dielectric (d, air or vacuum) exposed to laser wavelengths in the visible to IR spectral region, the condition for "SPP activity" can be simplified as $\mathrm{Re}(\epsilon_m) < -1$.[31,32] Particularly for irradiation with ultrashort laser pulses, this excitation channel is of major importance and may be enabled even for semiconductors and dielectrics as the initially plasmonically nonactive materials can transiently be turned into a metallic (SPP active) state, once a critical density of electrons in the conduction band is exceeded.[33,34]

An important remark must be made regarding the excitability of SPPs on flat surfaces that points back to the momentum conservation law: for a given laser frequency, a photon propagating in free-space has a smaller momentum than an SPP as the two have different dispersion relations that do not cross. This momentum mismatch is the reason why free-space photons from air/vacuum cannot couple directly to SPPs. Hence, some additional surface roughness is required to support the coupling of light to SPPs here, manifesting in the experimental observation that LIPSS are usually a multi-pulse phenomenon in the ablative regime. The first pulses ablate some material and generate a surface roughness that may facilitate the excitation of SPPs. This inter-pulse feedback mechanism during repetitive irradiations selects specific spatial periods of the roughness distribution that can better absorb the laser radiation.[35]

In the "standard SPP model of LIPSS," for simplicity the LIPSS (LSFL-I) period is directly linked through the SPP dispersion relation to its wavelength via $\Lambda_{LSFL} = \Lambda_{SPP}$. For the case of a plane dielectric–metal interface and for normal incident radiation, the latter can be calculated from the complex bulk dielectric permittivity of the metal (ϵ_m) and the dielectric (ϵ_d) and the laser wavelength λ as[29,31,36]

$$\Lambda_{LSFL} = \Lambda_{SPP} = \lambda \cdot \mathrm{Re}\left\{\sqrt{\frac{\epsilon_m + \epsilon_d}{\epsilon_m \epsilon_d}}\right\} \quad (1)$$

This approximation may hold for a small number of laser pulses when surface corrugations of the LIPSS are still small (modulation depths $h << \lambda$). However, once a sufficiently deep LIPSS relief is present at the surface, the simple expression of Λ_{SPP} given above is not valid anymore.[37,38] Thus, the applicability (surface modulation depth, interfacial SPP activity) of the simple "standard SPP model" always has to be checked carefully and is often questionable in the context of multi-pulse LIPSS experiments.

Variants of Equation (1) were used in different contexts to address the sub-wavelength characteristics of LIPSS (LSFL or HSFL) through changes in the dielectric permittivities. A straightforward approach lies in the modeling of the dielectric permittivity of the irradiated solid by a Drude model that predicts values of ϵ as a function of the number of laser-excited carriers in the conduction band (for semiconductors and dielectrics)[34,39–41] or even in sub-bands of the metallic band structure.[42] These intra-pulse changes can implicitly consider transient changes of the bulk optical properties of the material during laser irradiation. The model was applied also to layered systems treating the interfaces of films independently.[39] An extended thin-film-plasmonic model considering transient changes of the dielectric permittivities along with the electromagnetic coupling at the two interfaces was presented by Derrien et al.[43] Later it was transferred to oxidic films involved in the formation of a specific type of sub-ablative LIPSS on metals.[44]

The experimentally observed alignment of the LSFL relative to the linear beam polarization results from the directional excitation of the electrons of the material by the incident laser radiation. Depending on the electrical properties (metallic, dielectric), this leads to a directional radiation characteristic (radiative and nonradiative scattered fields, propagation) and, thus, to a specific, anisotropic field distribution of the induced SEWs.[45–47] In the case of plasmonically active materials, it should also be noted that the excitation of SPPs requires the irradiation of a transverse magnetic (TM) wave,[31] which causes the polarization dependence of LSFL, e.g., on metals.[34]

The SEW model can be extended to nonnormal incident radiation, where differences between s- and p-polarized light must be

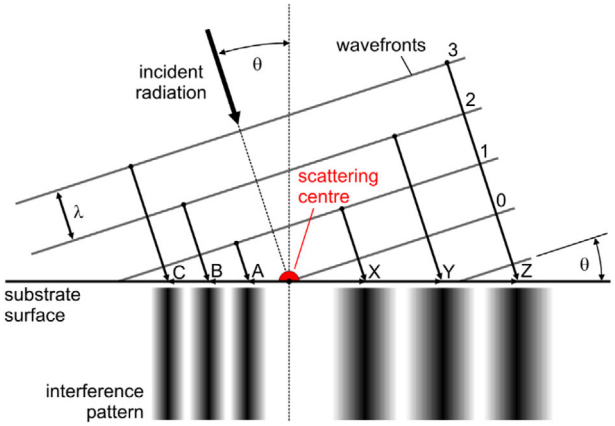

Figure 5. Interference of a p-polarized electromagnetic wave (wavelength λ) incident under the angle θ with an SEW generated by scattering at a defect (scattering center). The resulting interference pattern on the surface is characterized by different periods resulting from forward (increased) and backward (decreased) scattering (see Equations (2a) and (3a)). (Inspired by Figure 4 in Emmony et al.[48]).

considered. Depending on the angle of incidence θ, the orientation of the polarization with respect to the plane of incidence (s, p), and the dielectric permittivity of the solid ϵ, the LSFL-I period was predicted to follow the relations[27]

$$\Lambda_{\mathrm{LSFL,p}} \sim \frac{\lambda}{\xi \pm \sin\theta} \tag{2a}$$

and

$$\Lambda_{\mathrm{LSFL,s}} \sim \frac{\lambda}{\sqrt{\xi^2 - \sin^2\theta}} \tag{2b}$$

with $\xi^2 = |\mathrm{Re}(\epsilon)|/[|\mathrm{Re}(\epsilon)| - 1]$. For strong absorbing and plasmonically active materials [$\mathrm{Re}(\epsilon) << -1$], these equations simplify to

$$\Lambda_{\mathrm{LSFL,p}} \sim \frac{\lambda}{1 \pm \sin\theta} \tag{3a}$$

and

$$\Lambda_{\mathrm{LSFL,s}} \sim \frac{\lambda}{\cos\theta} \tag{3b}$$

The two branches of Equations (2a) and (3a) can be understood when considering that an SEW generated by scattering the obliquely incident radiation at a defect of the substrate surface creates one geometrical branch of radiation that is scattered partly in forward direction, while the other branch is scattered partly in backward direction (see **Figure 5**).

The interference of the incident p-polarized wave with the SEW scattered at the defect then results in an increased (forward scattering) and a decreased (backward scattering) period of the resulting interference patterns.

Another approach for considering changes of the dielectric permittivities in Equation (1) or (2) is based on the effective medium theory. Hwang and Guo[49] proposed the use of modified values of ϵ_{d} and ξ to consider the nanoscale roughness of the air exposed LIPSS-covered surface. This was implemented by the Maxwell–Garnett theory modeling metallic nanostructure inclusions to the dielectric host air[50] for explaining deviations between the predictions of Equation (2a) from fs-laser irradiation experiments of Au and Pt.[49] Later, this effective medium approach was combined also by a Drude model.[51,52]

Direct evidence for the involvement of SPPs in the LSFL-I formation was presented in complementary experimental approaches revealing the resonant absorption of radiation in prestructured surface gratings if SPPs can be excited. Garrelie et al. subjected a set of 10 nm shallow photolithographically manufactured linear surface gratings on nickel with discrete periods ranging between 440 and 800 nm to normal incident TM (polarization perpendicular to grating ridges) or transverse electric (TE)-polarized (polarization parallel to grating ridges) single 150 fs laser pulses with a center wavelength at $\lambda = 800$ nm.[36] Subwavelength-sized LSFL-I were produced for resonant grating coupling of TM-polarized radiation, confirming the predictions of Equation (1) when considering the transient changes of the dielectric permittivity of nickel. Later, Miyaji et al. used 66 nm deep photolithographic linear surface gratings of 1300 nm period on silicon in single-pulse excitation experiments ($\lambda = 800$ nm, $\tau = 100$ fs) with orthogonal (s-/p-) polarization directions and different irradiation fluences.[53] Upon variation of the angle of incidence (θ), a pronounced surface reflectivity dip manifested at a resonance angle of ≈24° only for the p-polarized radiation (TM-geometry) and at laser fluences sufficient to transiently turn the silicon into an SPP-active metallic state (see the statement above). Simultaneously, the post-laser irradiated grating depth increased to ≈400 nm, confirming the increased absorption through the grating-assisted SPP coupling. Complementary rigorous coupled-wave analysis (RCWA) simulations indicated an electromagnetic near-field enhancement through the SPPs at the geometrical edges of the grating ridges. Such polarization-dependent near-field enhancement effects at the grating-like surface topography may additionally facilitate the local material removal.[54,55]

3.1.2. Sipe's Theory

The currently most widely accepted theory on LIPSS was developed already during the eighties of the past century at the university of Toronto (Canada) in the group of van Driel and Sipe. Starting in 1982, this group published a series of pioneering papers[16,18–21] involving LIPSS formation experiments[16,19,20] on various materials using ns-lasers along with a detailed electromagnetic theory.[18,45] At the same time, important contributions were made by the group around Fauchet and Siegman, who developed an alternative scattering/interference-based approach.[17,22]

Starting from Maxwell's equations and using the Green's formalism, the work of Sipe and co-workers (in the following denoted for brevity as "Sipe theory") develops an integral equation of the dielectric polarization density at a microscopically rough surface, representing a general scattered-field model. It includes the possible excitation of SEWs (e.g., in the particular form of SPPs) and their interference with the incident radiation. Sipe's theory predicts possible wave vectors $\boldsymbol{k}$ of the LIPSS (related to

their period via $|\boldsymbol{k}| = 2\pi/\Lambda$) as function of surface parameters (surface roughness and bulk dielectric permittivity ϵ) and laser irradiation parameters (wavelength, polarization direction, angle of incidence θ). The theory provides an analytical expression for the inhomogenous deposition of optical energy into the irradiated material, written as

$$\text{Absorption} \sim \eta(\boldsymbol{k}) \cdot |b(\boldsymbol{k})| \quad (4)$$

The scalar response function η describes the efficacy with which the surface roughness (represented by $\boldsymbol{k}$) can absorb optical radiation. The second factor b is a scalar measure of the surface roughness at $\boldsymbol{k}$. For a nonirradiated (nonrippled) surface, b is usually a slowly varying function with homogenously distributed spatial frequencies of the roughness.[18] Opposed to b, the efficacy factor η may exhibit pronounced sharp peaks at specific $\boldsymbol{k}$ values, which can be used to evaluate the associated spatial periods Λ. LIPSS are observed where the efficacy factor η exhibits strong variations, which are usually associated with its maxima/minima. Once LIPSS are formed, b will exhibit sharp peaks as well that further reinforce the surface rippling via redistribution of optical energy from subsequent laser pulses. In other words, positive feedback can occur. However, it must be underlined here that this inter-pulse feedback is not explicitly included in the Sipe theory.

The pioneering publication[18] is not very convenient to use for the quantification of the efficacy factor for specific material and irradiation parameters. This drawback was removed by Bonse and co-workers, who published in 2005 a mathematical reformulation of η (without changing its validity range) as a set of 14 complex-valued equations.[56] That set of equation allows a straightforward calculation of η for s- or p-polarized radiation at the wavelength λ for a given dielectric permittivity ϵ, angle of incidence θ, and two roughness parameters s and F encoding the topographical characteristics of the rough surface. The "standard values" of s and F are 0.4 and 0.1, respectively, as derived by Sipe and co-workers for surfaces with spherically shaped islands acting as scattering centers for the incident optical radiation.[18]

On materials strongly absorbing the laser radiation such as metals and semiconductors, Sipe's theory typically predicts two dominant sickle-shaped features, which represent the LSFL (type LSFL-I)[15] with spatial periods close to the laser wavelength ($\Lambda_{\text{LSFL-I}} \sim \lambda$) and oriented perpendicular to the linear laser beam polarization (see Figure 1a). If the material is plasmonically active at λ, the peaks in η are very narrow due to the resonant absorption of the radiation.

On transparent dielectrics, another dominant type of LSFL (type LSFL-II)[15] is predicted. These structures exhibit subwavelength periods close to $\Lambda_{\text{LSFL-II}} \sim \lambda/\text{Re}(\sqrt{\epsilon}) = \lambda/n$ (with n being the refractive index of the material) and are oriented parallel to the laser beam polarization (see Figure 1c). In Sipe's theory, LSFL-II are related to so-called radiation remnants (RR) and originate from a specific nonpropagating electromagnetic mode close to the rough surface.[45] The latter is able to redistribute energy from the incident radiation transferring it to the material at specific spatial frequencies of the surface roughness.

The dominance of this RR absorption channel over that of the SEW feature for a rough surface of a low-index dielectrics is exemplified in **Figure 6**, where the respective maximum η_{max} of the two different LSFL-features is compared and plotted for a (fictive) nonabsorbing material of varying refractive index ($n = \text{Re}(\sqrt{\epsilon}) \in \mathfrak{R}$) that is irradiated at 800 nm wavelength.

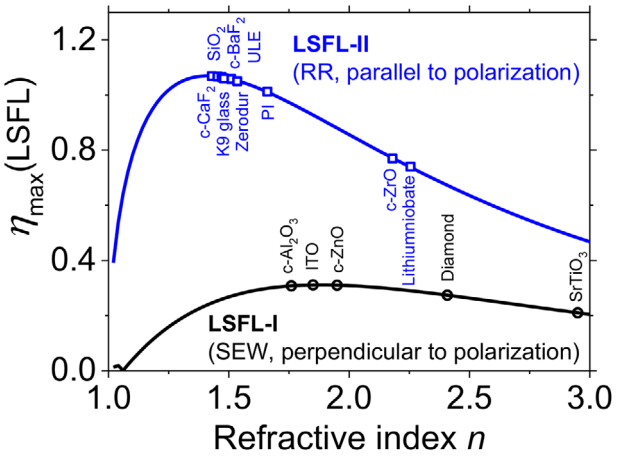

Figure 6. Maximum values η_{max} in the efficacy factor map calculated for LSFL-I and LSFL-II features as a function of the refractive index n of a (fictive) nonabsorbing dielectric material using $\theta = 0°$, $s = 0.4$, $F = 0.1$, and $\lambda = 800$ nm (solid lines). LSFL types and orientations experimentally verified on different materials are assigned on the two curves as open circles/squares at their corresponding n values.

A direct comparison of the curves of both LSFL features reveals that both, the maximum amplitude of η_{max} and the corresponding refractive indices are different: while η_{max}(LSFL-I, black line) stays below ≈0.3 at a refractive index of $n \sim 1.8$, η_{max}(LSFL-II, blue line) reaches more than three times larger values of ≈1.075 at a lower value of $n \sim 1.45$. In other words, a larger energy deposition is predicted by Sipe's theory for the LSFL-II structures, particularly for low refractive index dielectric materials. The dominance of the LSFL-II structures with periods close to λ/n and oriented parallel to the laser beam polarization manifests experimentally particularly for low-index dielectrics with large bandgap energies (requiring multi-photon absorption to be involved).[5,57–61]

The most prominent example is the material silicon dioxide in the form of amorphous fused silica or single-crystalline quartz. At 800 nm wavelength, their refractive index ($n = 1.453$) matches well the position of η_{max}(LSFL-II), see Figure 6. It was shown in a series of publications that the experimentally observed LSFL-II are seeded in the transparency regime of the material through an interplay of the microscopic surface roughness causing far-field scattering and interference with the laser radiation propagating in the material (see Section 3.1.3 and Rudenko et al.[46]) and sub-surface incubation effects. The latter are triggered by the excitation of *self-trapped excitons* as indicated in time-resolved trans-illumination pump-probe diffraction experiments.[4] The LSFL-II then finally manifests as surface relief upon multi-pulse irradiation.[61]

While the polarization direction, the angle of incidence, and the surface roughness of the nonirradiated surface usually can be considered as constant during the laser processing, the dielectric permittivity ϵ can undergo large changes—particularly when semiconductors or dielectrics are irradiated by high-intensity laser pulses allowing multi-photon absorption processes. For these materials, a transient metallization of the surface may

occur, potentially featuring SPP activity. The effect occurs if a sufficient number of valence band electrons of the solid is promoted via interband transitions into its conduction band (CB). The associated changes of ϵ then occur during the laser pulse and, hence, represent an intra-pulse feedback process. This mechanism was studied in detail by Bonse and co-workers in 2009 for two different materials, who combined the Sipe theory with a simple Drude model allowing to quantify the change of ϵ as a function of the number density of electrons N_e promoted into the CB of zinc oxide[62] or silicon.[33,63] This extension of Sipe's theory is called *Sipe-Drude model* and was later adopted for other materials.[61,64–70]

At normal laser beam incidence ($\theta = 0°$), the Sipe-Drude model reveals that for increasing electron densities in the CB of semiconductors[33,68] or dielectrics,[61,62] the LSFL-II (RR) feature changes its shape/position and finally diminishes, while the LSFL-I (SEW/SPP) feature becomes very pronounced with large amplitudes, once the irradiated material turns plasmonically active through an increased extinction. At very high values of N_e, all peaks disappear and η becomes widely constant and approaches zero. This is fully in line with the experimental observation that LIPSS are formed solely in a certain excitation (fluence) regime close to the damage/ablation threshold of the material.

An impressive experimental proof of Sipe's theory was published in 2010 by a group of scientists around Sokolowski-Tinten, who investigated the temporal dynamics of the formation of LIPSS on rough silicon films through fs-time-resolved coherent XUV scattering experiments in transmission geometry.[24] Without any adjustable parameter, almost quantitative agreement between the theoretically predicted efficacy factor and the experimentally recorded spatially scattered XUV-radiation pattern was found.

3.1.3. Finite-Difference Time-Domain (FDTD) Simulations

The FDTD calculations represent a method to numerically solve Maxwell's equations for specific geometrical boundary conditions. The method was introduced in 1966 by Yee.[71] With the increase of available computational power, it gained attraction as it allows to calculate the electromagnetic fields in the vicinity of nano- and microstructures. Based on the universality of the approach, it includes laser beam propagation effects, field enhancement, optical scattering, and interference phenomena and can be used to reveal spatio-temporal intensity distributions. Starting in 2012, some pioneering works in the context of LIPSS were published by Skolski and co-workers, who computed the inhomogenous energy absorption of fs-laser-irradiated silicon below the rough material surface.[72,73] The sample roughness was considered by adding an ensemble of randomly distributed topographic defects as an additional "roughness layer" on a plane surface. In the FDTD approach, the electromagnetic scattering, diffraction, and reflection at such rough surfaces as well as beam propagation effects are considered by implementing a single, spatially coherent ultrashort pulsed light source. Note that for obtaining meaningful results of the electromagnetic field distributions, averaging over several simulations with statistically varying surface roughness is usually required to check and confirm their physical relevance and to allow a comparison to analytic calculations and experiments.

Through Fourier transforms of their FDTD calculations of the spatial patterns of the energy absorbed from the laser beam, Skolski et al.[72] confirmed the validity of the earlier near-surface Sipe-Drude simulations,[33] as exemplified in **Figure 7** for weakly laser-excited crystalline silicon. This comparison between the FDTD and the Sipe-Drude approaches was recently extended to nonnormal incident laser radiation.[63]

The FDTD calculations are able to overcome some limitations of the Sipe theory by allowing to investigate even deeper lying sub-surface regions. The work of Skolski et al.[72] along with the one of Déziel et al.[74] provided a classification of a variety of LIPSS as the "fingerprint" of light scattering and localized absorption, named "type-d" (dissident, manifested as LSFL-II in dielectrics and semiconductors), "type-s" (scattering, manifested as LSFL-I in semiconductors and metals), "type-m" (mixed, predicted feature), and "type-r" (roughness dependent, represented by HSFL-I) (see **Table 1**). Periodic supra-wavelength-sized so-called "grooves" parallel to the laser beam polarization are labeled "type-g."[63,75]

Zhang et al.[76] extended the FDTD approach also to metallic and plasmonically active materials and identified the contribution of the scattered near-field and far-field on the types of inhomogenous energy absorption features. They found that the inhomogenous energy absorption, which triggers LSFL formation (type-s and type-d), results from the coherent superposition of the scattered far-field and the propagating (refracted) laser beam. In contrast, HSFL-I (type-r) originates from the coherent superposition between the scattered near-field and the propagating (refracted) beam.

In 2014, Skolski et al. additionally implemented inter-pulse feedback by combining their FDTD approach with a basic material removal (ablation) criterion.[73] This allowed to construct a carrier density and ablation depth-dependent "morphological map" of a plethora of HSFL, LSFL, and admixtures of both being parallel or perpendicular to the laser beam polarization. Déziel et al.[77] extended that FDTD-feedback simulations to account for expansion-like mechanisms in the LIPSS formation process as they may be involved in sub-ablative conditions via hydrodynamic melt-flows. This allowed to explore the growth of a larger class of nanostructure surface morphologies, including LIPSS on dielectrics and metals.

Recently, Zhang et al.[63] reported in such inter-pulse feedback FDTD simulations of fs-laser-irradiated chromium a "type-2s" feature that may be observed together with the type-s one. It represents LIPSS with strictly half the period of that associated with the type-s feature. It was attributed to the redistribution of the electric field due to the previously formed LSFL-I topography.[63,78] Such an effect of LSFL-I ridge splitting was reported before already for fs-laser irradiation experiments on steel[79] and manifests in a narrow fluence range only. Table 1 summarizes the characteristics and origin of these features.

The FDTD approach of Zhang et al.[63] confirmed the earlier experimental finding that LIPSS can be used as probe of the local polarization state.[80–82] This was demonstrated by the use of so-called optical vortex beams, which allow to create focused laser beams with varying polarization states localized in complex spatial fluence distributions.[83] This is visualized in **Figure 8**, which

Table 1. Classification of different types of LIPSS summarizing their characteristics (orientation to polarization, spatial period Λ), their qualitative representation in Fourier space, and the materials involved. The two dashed circles in the Fourier space mark spatial frequencies $|\kappa| = \lambda/\Lambda = 1$ and $|\kappa| = \lambda/\Lambda = \mathrm{Re}(\sqrt{\epsilon})$.

Classification origin	Orientation	Period Λ	Representation in Fourier space	Type of LIPSS	Materials
Type-s SEW, SPP, radiative fields	$\perp$	$\approx\lambda$	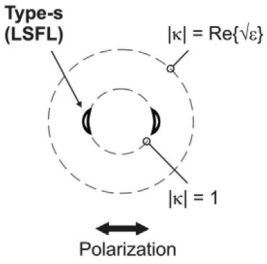	LSFL-I	metals, semiconductors
Type-d RR, "far-field" scattering, radiative fields	$\parallel$	$\approx\lambda/\mathrm{Re}(\sqrt{\epsilon})$	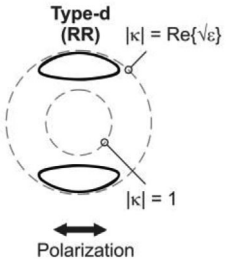	LSFL-II	semiconductors, dielectrics
Type-m RR	$\parallel$	$\approx\lambda$	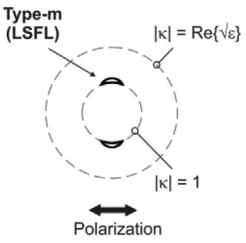	LSFL	
Type-r near-field scattering, nonradiative fields	$\perp$	$\approx\lambda/[2\mathrm{Re}(\sqrt{\epsilon})]$	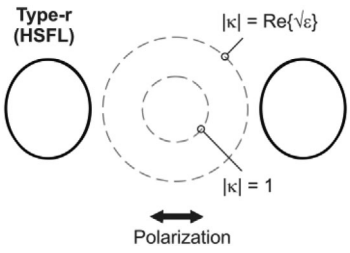	HSFL-I	semiconductors, dielectrics
Type-2s SEW, SPP with electric field redistribution	$\perp$	$\approx\lambda/2$	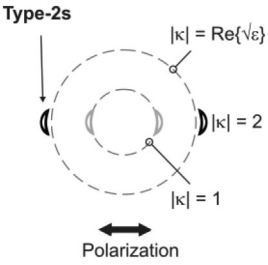	split LSFL-I	metals, semiconductors
Type-g scattering	$\parallel$	$> \lambda$	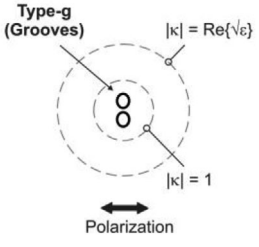	grooves	metals, semiconductors

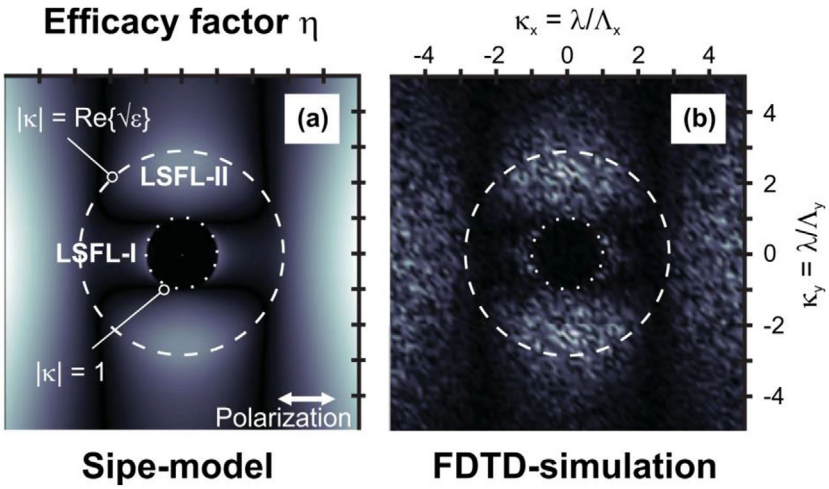

Figure 7. Direct comparison of the analytic Sipe theory with numeric FDTD-simulations. a) η (Sipe-model) and b) FDTD-η maps computed with $\theta = 0°$, $\lambda = 800$ nm, and $(F,s) = (0.1,0.4)$. The maps are obtained for weakly laser-excited silicon ($N_e = 2 \times 10^{21}$ cm^{-3}, $\sqrt{\epsilon} = 2.868 + 0.382i$). The polarization direction is indicated by the white arrow in (a). The dotted and dashed circles represent $|\kappa| = 1$ and $|\kappa| = \mathrm{Re}(\sqrt{\epsilon})$, respectively. A linear grayscale color map is used, the brightest areas represent the largest values. The noise in (b) arises from the fact that the FDTD-simulation was performed with a discrete, randomly distributed rough surface. Reproduced with permission.[72] Copyright 2012, American Physical Society.

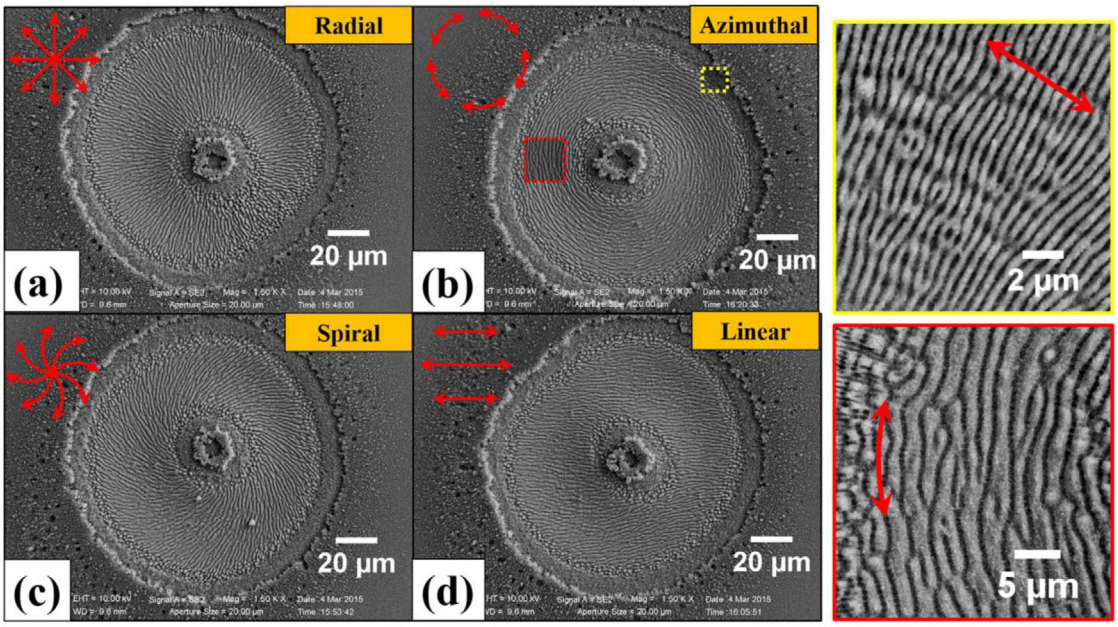

Figure 8. SEM images of surface morphologies on a silicon wafer irradiated by four different optical vortex beams all featuring a doughnut-like intensity profile along with a a) radial polarization pattern, b) azimuthal polarization, c) spiral polarization, and d) linear polarization. The two panels on the right illustrate the fine morphology of the surface structure generated by the azimuthal polarization pattern ($\lambda = 800$ nm, $\tau = 35$ fs, $E = 48$ μJ, $N = 100$, $\theta = 0°$). The grooves dominating the structured areas are always parallel, while the LSFL-I are strictly perpendicular to the local beam polarization. Reproduced under the terms of a Creative Commons BY 4.0 license.[81] Copyright 2015, The Authors, published by Springer Nature.

shows top-view scanning electron microscopy (SEM) images of silicon wafer surfaces that were irradiated by 100 consecutive fs-laser pulses at normal incidence, featuring a) radial, b) azimuthal, c) spiral, and d) linear polarization states. Two different types of LIPSS can be seen in these images: micrometric grooves (type-g feature) dominate the structured surface areas and are always parallel to the local laser polarization, while the sub-micrometer LSFL-I (type-s feature) are strictly perpendicular to it.

Recently, FDTD simulations provided the theoretical base of the link between the HSFL-I and the subwavelength volumetric nanogratings formed in the bulk of dielectrics.[84–86] While the experiments of Hörstmann-Jungemann et al.—moving the focus

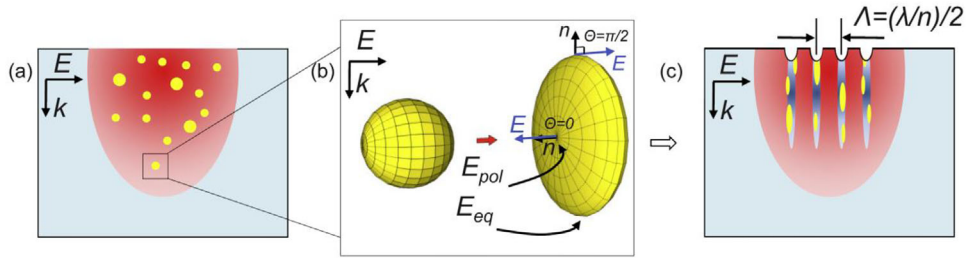

Figure 9. a) Localized nanoplasmas (yellow) formed in the bulk of the fs-laser-excited (semi-)transparent material (red). b) Nanoplasma growth into planes by local field distribution and periodic plasma sheet formation, for details refer to Buividas et al.[88] c) Formation of HSFL-I at the surface via optical breakdown and ablation. Reproduced with permission.[88] Copyright 2011, IOP Publishing.

of a tightly confined laser beam from the volume (bulk) to the surface of the irradiated transparent material—pointed already in 2009 toward a joint physical origin,[87] the theoretical explanation was missing for a long time.

A first adoption of a theoretical model of volumetric nanogratings to surface ripples on (semi)transparent materials was presented by Buividas et al. in 2011.[88] In this approach, the HSFL are formed from plasma nanospheres localized in the bulk of the irradiated material at the pre-breakdown conditions, i.e., when the global electron plasma density is lower than the critical value. The surface ripples are then pinned to the smallest possible standing wave cavity inside the material of refractive index n, defining the corresponding HSFL-I period $\Lambda = \lambda/(2n)$, sketched in **Figure 9**. Later, this idea was further explored by means of the 3D-FDTD calculations with seeding scattering centers located at the surface, as summarized in the following.

As pointed out by Rudenko et al.[46] for dielectrics, both nanostructures (type-r HSFL-I and volume nanogratings) share the same formation mechanism and originate from the interference between the incident electromagnetic field and the nonradiative near-field coherently scattered at surface defects. This intra-pulse scattering process does not require the fs-laser-irradiated dielectric to turn entirely into a metallic state. It relies on the existence of nanoscopic local defects that promote locally enhanced absorption, field-enhancement, and scattering. The spatial period of the HSFL-I is usually close to $\lambda/[2n] = \lambda/[2\mathrm{Re}(\sqrt{\epsilon})]$. In contrast to the HSFL-I, the type-d LSFL-II with periods of $\sim\lambda/n = \lambda/\mathrm{Re}(\sqrt{\epsilon})$ are seeded a few hundreds of nanometers below the surface by the interference of the incident light with the radiative scattered fields, decaying slower (i.e., with $\approx 1/r$, r: radial distance)[89] than the nonradiative near-fields (decaying with $\approx 1/r^3$)[89] for increasing depths from the surface. Via repetitive fs-laser irradiation and incubation effects (inter-pulse feedback), the LSFL-II become visible at the surface once the covering near-surface material is removed through ablation. Note that the depth at which the LSFL-II are formed in dielectrics is located in the *radiative intermediate region* that is separating the regimes of nonradiative *near-field scattering* [$r < \lambda/(2\pi)$] and radiative *far-field scattering* [$r > 2\lambda$].[89]

That scenario is illustrated in the collage presented in **Figure 10**. In the SEM micrograph shown in Figure 10c, LSFL-II appear in the center at the bottom of the ablation crater formed in silica after irradiation by 20 consecutive fs-laser pulses with a spatially Gaussian beam profile at 5.8 J cm^{-2} peak fluence. Within an annulus around the LSFL-II-covered center the HSFL-I are present close to the sample surface. Figure 10a,b,d,e provides the corresponding calculated electron density profiles—colored as a function of depth in (d) or encoding the normalized electron density in (a), (b), and (e)—where the co-existing spatial signatures of the LSFL-II and HSFL-I are evident. Their orthogonal orientation is finally a consequence of the spatial scattering characteristics of sub-wavelength surface defects along with the optical properties of the irradiated material (dielectric vs metallic, see Fig. 2 in Rudenko et al.[46]).

As most dielectric materials exhibit a pronounced incubation behavior, the appearance of specific types of LIPSS, caused by the electromagnetic scattering mechanisms discussed above, and the transition among these different types can be strongly influenced by the number of pulses applied per spot and the incident laser fluence values. **Figure 11** exemplifies the LIPSS formation behavior of the ps-laser-irradiated polymer polycarbonate.[90] The schematic can act as archetype for other dielectric materials.

In 2019, Rudenko et al.[47,91] applied their combined approach, i.e., the electromagnetic 3D-FDTD model coupled with a hydrodynamic model (see Section 3.2), to a metal in order to simulate theoretically the topographic transition from a randomly rough steel surface to a quasi-periodic sub-wavelength grating upon irradiation with multiple ultrashort laser pulses (λ = 800 nm, τ = 160 fs, N = 0–100, ϕ_0 = 0.5 J cm^{-2}, θ = 0°).

Starting from a flat surface that is randomly covered by nanoholes (semisphere shaped voids of 10 nm diameter with an average spacing of 100 nm) and at incident laser fluences in the ablation regime, the authors tracked the pulse number evolution of the LSFL-I and their geometrical characteristics, see **Figure 12**.

The FDTD analysis of a single sub-wavelength hemispherical hole in the steel surface exhibits a pronounced broad-frequency electromagnetic field-enhancement at distances $\lambda/2$–λ regardless of the nanometric holes diameter, depth, or shape. When considering a large set of such nanoholes interacting collectively, the numerical simulations revealed the transition from a statistically rough surface to well-ordered quasi-periodic LSFL-I structures through multi-pulse ablation feedback based on electromagnetic scattering. As previously reported in experiments for strong absorbing materials,[92–94] the spatial LIPSS period $\Lambda_{\mathrm{LSFL\text{-}I}}$ then reduces with an increasing number of laser pulses per irradiated spot, finally saturating at values around $3\lambda/4$ in the center of the ablated spot,[47] see **Figure 13**.

In more detail, the decrease in LSFL-I periods was attributed to the reinforced dipole–dipole coupling between the nanoholes that is affected by the complex interplay of both, the excitation of

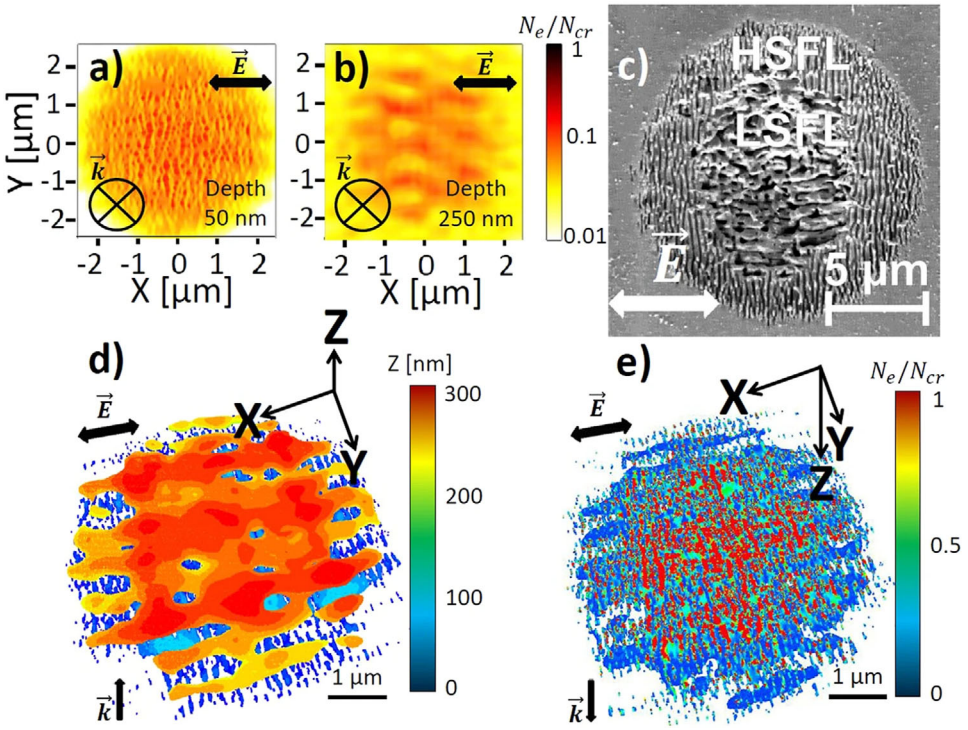

Figure 10. Electron density distributions in silica calculated by 3D-FDTD-simulations at the temporal maximum of a 2 μJ, 120 fs laser pulse at 800 nm wavelength. Normalized in-plane electron density distribution at a depth of a) 50 nm and b) 250 nm from the rough silica/air interface. c) SEM micrograph of a spot on a quartz surface irradiated by multiple fs-laser pulses (λ = 800 nm, τ = 150 fs, ϕ_0 = 5.8 J cm^{-2}, N = 20, f = 0.15 kHz, θ = 0°) in air. d) Electron density profiles colored as a function of depth (z). e) Electron density profiles colored as a function of normalized electron density. $\vec{E}$ marks the direction of the polarization. Reproduced under the terms of a Creative Commons BY 4.0 license[46] Copyright 2017, The Authors, published by Springer Nature.

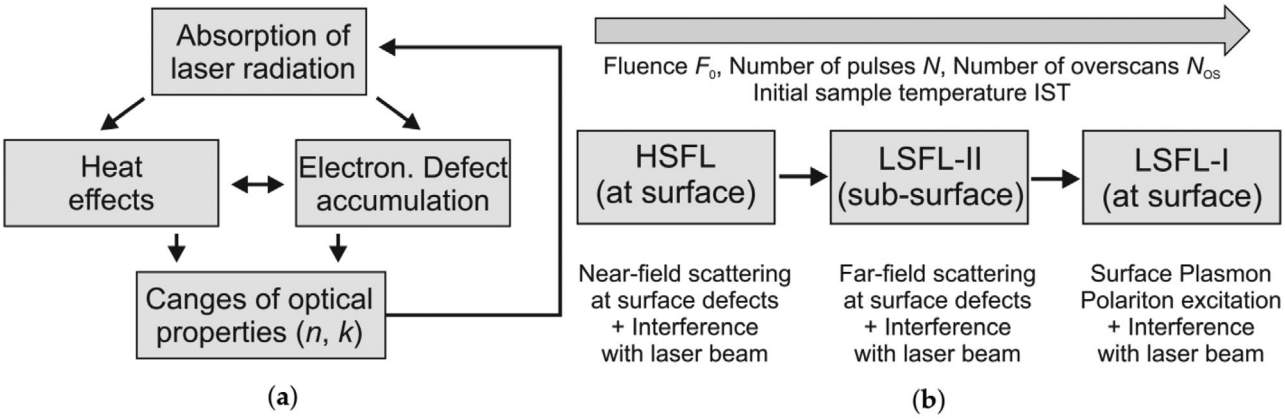

Figure 11. a) Scheme of iterative intra-pulse effects changing the optical properties of a dielectric (polycarbonate) during laser irradiation. b) Scheme of the evolution/transition between different types of LIPSS at the surface of dielectrics. Reproduced under the terms of a Creative Commons BY 4.0 license.[90] Copyright 2019, The Authors, published by MDPI.

SPPs and that of quasi-cylindrical surface waves.[29,47] The collective electromagnetic response of the set of nanoholes then promotes a pronounced shift toward lower periods with an increasing nanohole concentration generated upon laser ablation.

The work of Rudenko et al.[47] made an important contribution to the debate of the sub-wavelength characteristics of the LSFL-I as it presented convincingly the first model covering for each individual pulse irradiation the complete timespan from the early laser excitation up to the re-solidification, coupled via a pulse-to-pulse feedback loop.

With the help of FDTD, even more complex situations than surfaces of different classes of bulk materials can be investigated. This was recently demonstrated by Florian et al.,[95] who investigated the impact of a (laser-induced) oxide layer formed at the

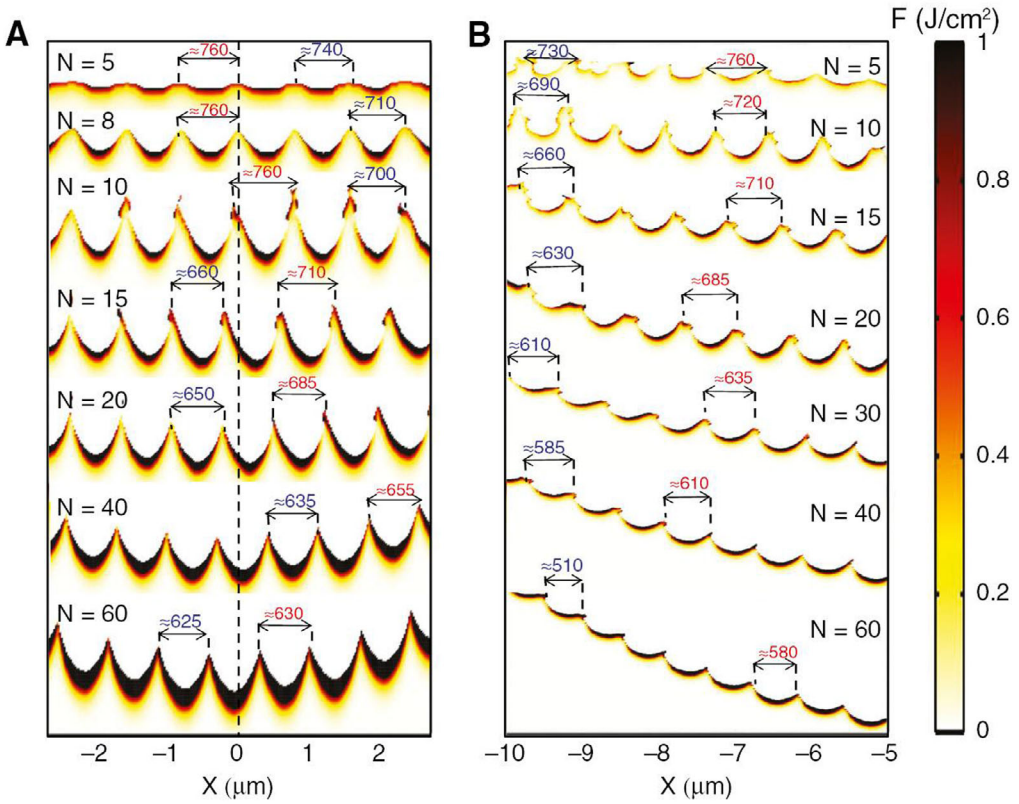

Figure 12. Evolution of ripple periods under multi-pulse irradiation. Absorbed fluence (F) distribution after irradiation of a stainless steel surface with pristine roughness (scattering holes of radius $R = 10$ nm and average spacings $d = 100$ nm) by N laser pulses with a laser peak fluence of 0.5 J cm^{-2} a) at the center and b) at the edges of the ablation crater. Reproduced under the terms of a Creative Commons BY 4.0 license.[47] Copyright 2019, The Authors, published by De Gruyter.

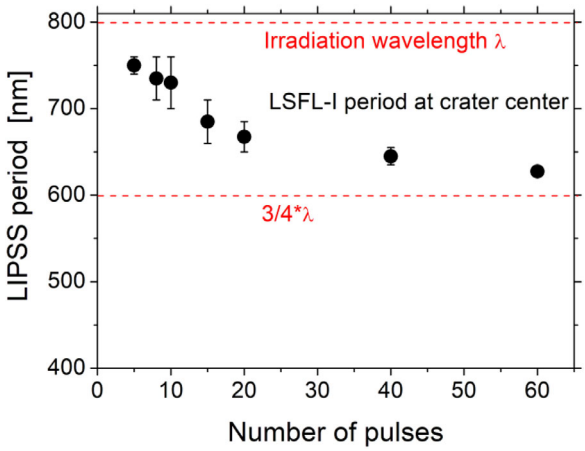

Figure 13. Pulse number dependence of the LSFL-I period evaluated from Figure 12 at the crater center positions.

surface of oxidation prone, strongly absorbing materials (such as a CrN ceramic, see **Figure 14**). It was demonstrated experimentally and by FDTD simulations that an oxide layer of ≈100 nm thickness strongly influences the formation of a regular intensity pattern at the interface to the underlying material that finally leads to the formation of the interfacial LSFL-II structures parallel to the laser beam polarization. The intensity pattern carrying that LSFL characteristics (type-d) is formed via the joint action of coherent electromagnetic scattering, propagation, and interference effects. It does not even require the presence of nanoplasmas scattering from localized defects or a partially metallic oxide layer (via laser-excited conduction band electrons).

3.1.4. Particle-in-Cell (PIC) Simulations

The ability of high-intensity ultrashort laser pulses to drive the electronic system of a solid into a state not being in equilibrium with the lattice and to induce a collectively coupled behavior of these electrons (such as in SPPs) allows to adapt methods that were initially developed in the field of plasma physics. One method proposed already in 1955—even before the broad availability of modern computers—is called PIC.[96] PIC relies on the calculation of trajectories of charged particles in self-consistent electromagnetic (or -static) fields that are computed on a fixed (Eulerian) mesh. The method typically implements interactively the following procedures: i) integration of the equations of motion that are including Lorentzian forces (solved by the "particle mover" code), ii) interpolation of charge and current source terms to the field mesh, iii) computation of the electromagnetic fields on the mesh points via Maxwell's equations (implemented through the "field solver" code), iv) interpolation of the electromagnetic fields from the mesh to the particle locations, etc. For

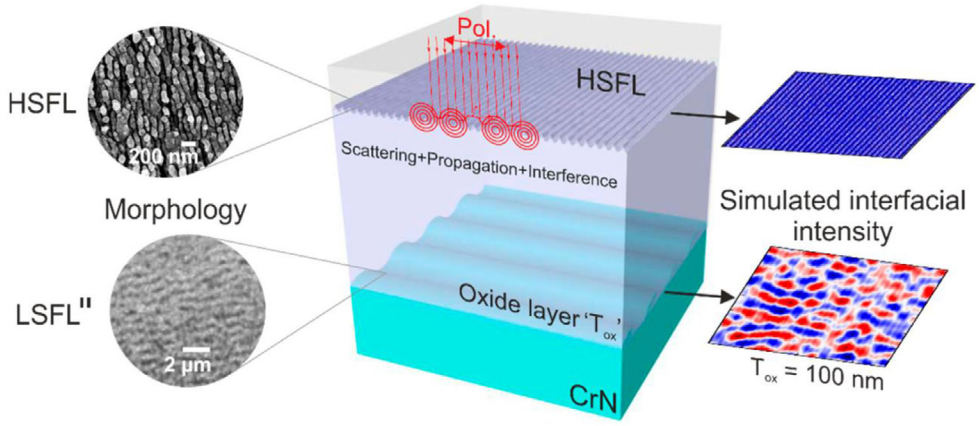

Figure 14. Scheme of the formation of interfacial LSFL parallel to the linear beam polarization in an oxidation prone material. Reproduced under the terms of a Creative Commons BY 4.0 license.[95] Copyright 2020, The Authors, published by MDPI.

reducing the complexity and the computational demands, clustered super-structures can be used (usually with $> 10^5$ particles). Nowadays, several commercial or open access PIC software implementations are available.[97]

So far, just a few groups have studied LIPSS on basis of PIC-simulations.[98–102] Djouder et al. simulated the irradiation of a copper target by linearly and circularly polarized fs-laser pulses (800 nm wavelength, 70 fs duration) at intensities up to 10^{16} W cm^{-2} in a relativistic 2D-PIC scheme.[98,99] Their results indicate the early signature of LIPSS for the linearly polarized radiation already appearing during the laser pulse, featuring a sub-wavelength characteristics. Later, Gouda et al.[100] used a relativistic 2D-PIC model considering a preformed hydrogen plasma (sub-critical, electron densities of $0.7 \times N_{crit}$) covering a super-critical hydrogen plasma ($10 \times N_{crit}$) upon fs-laser pulse irradiation (800 nm wavelength, ≈30 fs duration) at a peak intensity of 10^{16} W cm^{-2}. At such high (relativistic) laser beam intensities up to 10^{18} W cm^{-2}, the Weibel instability was attributed to be the dominant pattern formation mechanism in the laser-excited plasma, while at lower (nonrelativistic) peak intensities, ordinary surface plasma waves drive the pattern formation in the plasma electron density.[101] The latter scenario of the excitation of SEWs was confirmed in more detail by Russel, who modeled by 2D-PIC the coupling of a focused spatially Gaussian fs-laser beam (800 nm, 0.5–3.0 J cm^{-2}, 60 fs, $w_0 \sim 1$–8 μm) to a plane copper surface with a single rectangular narrow groove.[102] These simulations revealed a strong near-surface field enhancement (≈175%) through the intra-pulse excitation of SEWs at the defect, associated with periods predicted by Equation (2a) and a coupling efficiency of ≈28%. Moreover, it was visualized that the SEWs are solely driven during the laser pulse. After the pulse they may spatially propagate in a damped manner away from the defect.[102]

3.1.5. Two-Temperature Model (TTM)

One particularity of the interaction of fs-laser pulses with solids is caused by their extremely short pulse duration along with the fact that the intra-pulse absorption of the laser radiation occurs via the electrons of the solid. If the duration of the laser pulses is shorter than the *electron–phonon coupling time* ($\tau_{e\text{-}ph}$), i.e., the time required to transfer absorbed energy from the electronic system to the lattice of the solid, the absorbed laser pulse energy remains locally confined during the interaction and does not spread through heat diffusion into the area surrounding the laser-excited region. $\tau_{e\text{-}ph}$ depends on the material and is typically ranging between 0.1 and 10 ps. The electron–phonon coupling mechanism imposes some constraints on the formation of LIPSS, particularly the experimentally observed lower limit of spatial periods of the HSFL, which account to several tens of nanometers. As proposed by Bonse et al., this limit is caused by thermal diffusion effects that are washing out too small spatial modulations in the absorbed energy during the transfer of the energy from the optically excited electronic system to the lattice of the solid.[15] The question if a spatial modulation of the absorbed optical energy can "survive" the electron–phonon relaxation processes was already addressed by Derrien et al. with a model considering the interference of the laser irradiation with an SEW propagating on the surface of fs-laser-excited silicon, the associated laser energy absorption and free carrier formation, and subsequent energy relaxation via electron–phonon coupling.[103] This was numerically implemented through TTM.[104] Technically, the TTM is a pair of partial differential equations that are used to track the temporal evolution of the temperatures (electron temperature T_e and ion/lattice temperature T_i) of a system of interacting electrons and lattice ions, which are both in local thermal equilibrium among themselves but not with each other. With the surface situated at (x; $z = 0$) and z being the depth, the temporal evolution can be derived from[103,105]

$$C_e \frac{\partial T_e(t,x,z)}{\partial t} = \nabla \cdot \left(\kappa_e \nabla T_e\right) - \gamma_{ei}\left(T_e - T_i\right) + S(t,x,z) \tag{5a}$$

$$C_i \frac{\partial T_i(t,x,z)}{\partial t} = \nabla \cdot \left(\kappa_i \nabla T_i\right) + \gamma_{ei}\left(T_e - T_i\right) \tag{5b}$$

Here, the subscripts "e" and "i" are for electrons and ions/lattice, respectively. C represents the specific heat capacity, κ is the heat conductivity, and $\gamma_{ei} = C_e/\tau_{e\text{-}ph}$ is the electron–phonon coupling factor. The last term on the right side of Equation (5a) represents the source term $S(t,x,z)$ that accounts for the absorption of the laser pulse energy. In the case of fs-laser-irradiated semiconductors such as silicon, S may consider one- and two-photon absorption processes, impact ionization, and Auger recombination, finally imposing a spatial modulation of 800 nm period in the electron density and electron temperature profiles (through the interference between the laser beam and the SEW electromagnetic field), as well as the subsequent coupling of the electronic system and the lattice of the solid through electron–phonon coupling and thermal diffusion.[103] Later, this model was further improved and extended to consider additional effects such as electron diffusion and the phase transition of thermal melting.[106] Moreover, the authors transferred their model also to the case of a metal, i.e., fs-laser-irradiated titanium[106] and gold.[105] The TTM calculations confirmed that for both materials (semiconductors and metals) the spatial LSFL-I characteristics with typical periods of a few hundred nanometers are preserved during the electron–phonon coupling at laser fluences including the melting regime. It can be expected that this approach will be further extended to include i) sub-wavelength modulations mimicking the HSFL periods and ii) higher fluences associated with ablation, e.g., via adding the phase transition of thermal evaporation to the TTM model, and iii) dielectric materials. This may finally confirm/refute the above mentioned hypothesis of the origin of the lower limit of HSFL spatial periods. **Figure 15** schematically summarizes the physical processes considered in the TTM approach.

Finally, it should be noted that the TTM was already implemented as part of more complex LIPSS simulations based on FDTD (see Section 3.1.3) for dielectrics[46,107] and metals,[47] and in combination with hydrodynamic simulations (see Section 3.2.1) for metals,[92,108] semiconductors,[109,110] and dielectrics[111] and in molecular dynamics (MD) simulations (see Section 3.2.3) of metals.[112]

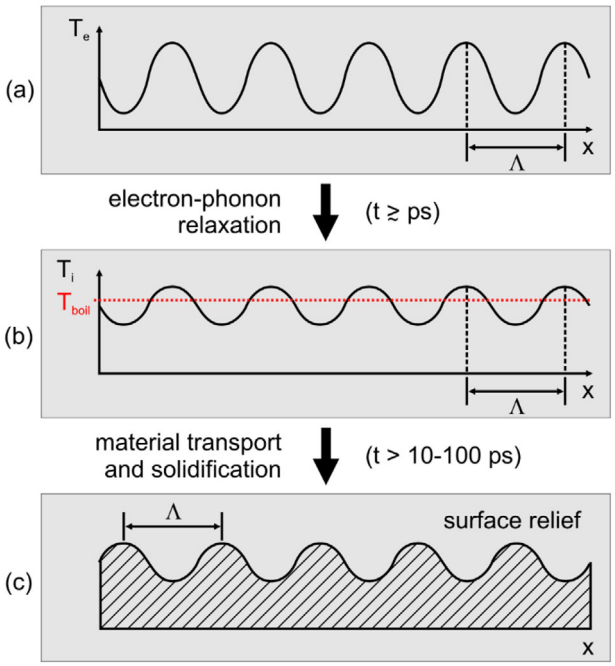

Figure 15. Scheme of LIPSS formation based on the two-temperature model (TTM): a) The interference between the laser beam and the SEW electromagnetic field is assumed to induce spatially modulated electron density and electron temperature (T_e) profiles with the period Λ. b) The subsequent coupling of the electronic system and the lattice of the solid through electron–phonon coupling and thermal diffusion leads to a modulated lattice temperature (T_i) profile that locally exceeds boiling temperature (T_{boil}). c) Selective ablation, material transport, and solidification result in the final LIPSS pattern (surface relief).

3.2. Matter Reorganization Theories

Matter reorganization theories rely on the transport of laser-excited material that reshapes the surface topography into a quasi-periodic ensemble of surface protrusions and depressions. Possible mechanisms involve thermodynamic phase transitions and hydrodynamic effects of the transiently melted surface (Section 3.2.1), material instabilities or microscopic accumulation such as defect creation, diffusion, or erosion effects (Section 3.2.2). A powerful numerical method for studying the reorganization of matter after the laser irradiation process is provided by MD simulations (Section 3.2.3).

All these theories are driven by local gradients and require the surface to stay long enough in an excited state that enables the underlying mechanisms to act at sufficiently large reorganization rates. Hence, these effects may dominate either for long pulse durations (exceeding several nanoseconds) or for a large number of laser pulses (reinforcing the topographical effect through the number of reorganization events triggered).

3.2.1. Hydrodynamic Theories

Early ideas connected the LIPSS topography to hydrodynamic effects that are frozen upon re-solidification of the laser-excited surface. Possible mechanisms were proposed to be based on surface tension gradients,[113] thermoelastically generated surface acoustic waves (SAWs),[114,115] or capillary waves (CWs).[27,116]

The idea behind the thermoelastically generated SAWs can be summarized as follows: the (linear) absorption of the laser radiation by the solid occurs in the near-surface layer (usually < 1 μm in depth). Within this layer, the deposited energy creates an exponential profile of the carrier density and lattice temperature and the associated strain field. The spatially varying strain field couples to SAWs of appropriate spatial frequency. For small laser spot sizes, a strong transversal component of the strain field is present then. Its spectrum of spatial frequencies can provide a propagating component of the SAWs. Phase transitions such as melting often involve discontinuous mass density changes (e.g., crystalline silicon densifies by a several percent upon melting). The spatio-temporal dynamics of the propagating melt-in or re-solidification front may additionally contribute to the excitation of SAWs.

The review article of Akhmanov et al.[27] presents a detailed analytical theory of the CW-based mechanisms by analyzing the general dispersion relation. Feedback is involved via the dependence of the surface tension coefficient on the temperature

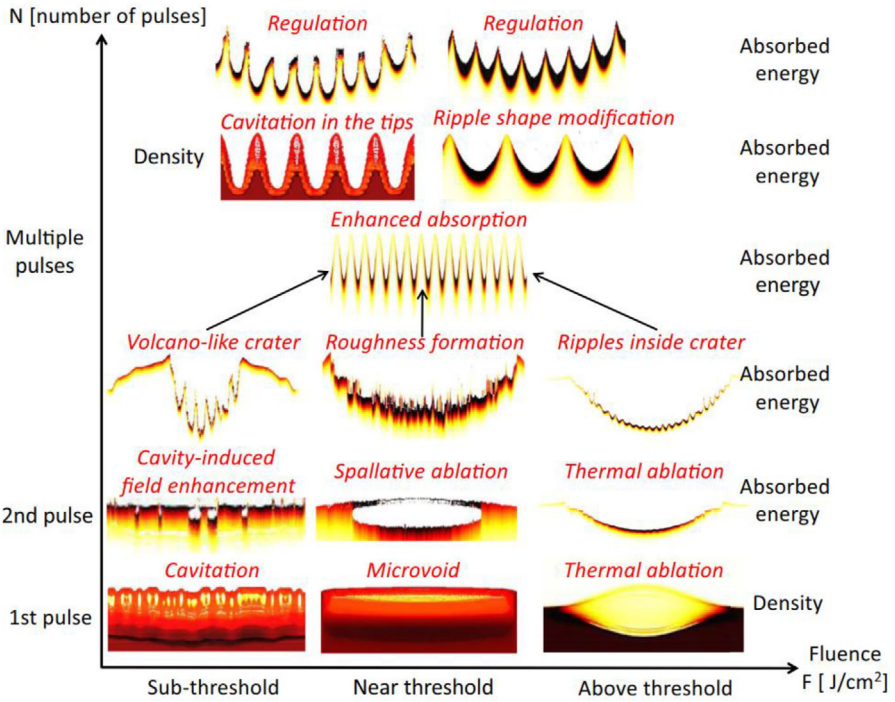

Figure 16. Color-encoded cross-sectional surface profiles calculated by combining hydrodynamic theories based on compressible Navier–Stokes equations with 3D-FDTD as a function of the applied number of laser pulses for three characteristic fluence ranges in the regimes below (left column), close to (middle column), and above the ablation threshold fluence (right column). Reproduced with permission.[91] Copyright 2019, American Physical Society.

(thermocapillary forces, *Marangoni effect*) or recoil pressure in spatially nonuniform evaporation, or SAWs.

Current hydrodynamic theories of LIPSS assume a molten (liquid) state of the irradiated material and then rely as central element on the Navier–Stokes equation (NSE)—a nonlinear partial differential equation that describes motion of a continuous fluid using vector fields of displacement velocities $\vec{u}$. From a physical point of view, the NSE considers the momentum conservation in hydrodynamic motions. The NSE has been formulated for both incompressible and compressible fluids. Equation (6) exemplifies the compressible NSE in Eulerian form implemented by Rudenko et al.,[91] which also includes near ablation threshold phenomena such as shock and rarefaction waves[117]

$$\frac{\partial\left(\rho\vec{u}\right)}{\partial t} + \left(\vec{u}\cdot\nabla\right)\left(\rho\,\vec{u}\right) + \left(\rho\cdot\vec{u}\right)\nabla\cdot\vec{u} = -\nabla P + \mu\nabla^2\vec{u} + \tfrac{1}{3}\mu\nabla\left(\nabla\cdot\vec{u}\right) \tag{6}$$

where ρ is the mass density of the liquid, μ is its dynamic viscosity. P is the pressure, taking into account electronic and lattice contributions, defined by the equation of state (EOS, for details see Rudenko et al.[91] and references therein). Together with properly set boundary conditions and in combination with the continuity equation

$$\frac{\partial\left(\rho V\right)}{\partial t} + \nabla\cdot\left(\rho\, V\,\vec{u}\right) = 0 \tag{7}$$

considering the mass conservation ($0 \leq V \leq 1$ is the fractional volume open to flow), the hydrodynamic flows at a surface melted upon laser irradiation can be computed in space and time.

In most recent approaches, hydrodynamic theories were numerically combined with electromagnetic theories of electromagnetic material excitation and heat transfer and its dissipation. Both, incompressible[109,110] and compressible NSE-based hydrodynamic approaches were developed,[91,108] for an assessment of the specific differences between both NSE models, see Section 4.2. Including multi-pulse feedback, some authors discussed a convection-role mechanism based on the Marangoni effect that may account for supra-wavelength periodic structures, such as supra-wavelength LSFL or grooves.[92,108,111,118]

However, when hydrodynamic theories based on the compressible NSEs are used in combination with a 3D-FDTD model, including as input the absorbed energy densities deposited by ultrashort laser pulses via electromagnetic scattering, many experimental findings can be reproduced.[91] **Figure 16** assembles these phenomena as plots of color-encoded cross-sectional surface profiles ordered via the applied number of laser pulses for three characteristic fluence ranges in the regimes below (left column), close to (middle column), and above the ablation threshold fluence (right column).

Using the same multi-physical approach (i.e., 3D-FDTD for solving the Maxwell equations, coupled with a TTM and compressible NSE, supported by the EOS), the same authors provided the missing explicit link between the electromagnetic and hydrodynamic LIPSS scenarios by elucidating in detail the role of different hydrodynamic instabilities following the electromagnetic

excitation processes of fs-laser-irradiated Nickel surfaces ($\lambda = 400$ nm/800 nm, 0.15–0.5 J cm^{-2}, $N = 1$–5, $\tau = 80$ fs, $\theta = 0°$).[108]

The simulations revealed that strong electromagnetic field enhancement at surface defects, local heat confinement, and the excitation of a sub-surface rarefaction wave trigger the Marangoni convection instability and finally result in the destabilization of a thin laser-induced melt layer. A polarization dependence of the hydrodynamic melt flows is imposed by the polarization dependence of the optical absorption in the vicinity of local bumps or surface holes that generate local temperature gradients and initial perturbations being asymmetric in the surface plane. No evidence for the involvement of *Rayleigh–Taylor instabilities* in the melt layer was found. In absence of polarization-dependent gradients in the melt, i.e., at fluences only slightly exceeding the melting threshold, quasi-hexagonal convection cells with sub-wavelengths dimensions were found—in accordance with experiments.[108]

Apart from identifying the relevance of the different physical mechanisms, these simulations also allowed to study the dynamics of the LIPSS formation. Particularly, it was shown that for laser fluences leading to HSFL-II, after the absorption and nonradiative scattering of the incident laser pulses at the rough surface (2% coverage with nanobumps and nanoholes of $R = 5$ nm radius), the interfacial melt-in and the counter-propagating rarefaction wave propagating through the excited material leads within 15–25 ps to destabilization of the system that initiates Marangoni flows. The latter shapes the HSFL pattern featuring periods between 60 and 180 nm and is most pronounced between 50 and 100 ps before interfacial solidification starts. Typical Marangoni numbers were estimated to be $Ma \sim 0.4$–2. The re-solidification process terminates about 250–500 ps after the laser excitation (depending on the laser fluence). It was concluded that for metals, the HSFL-II periods are imposed by hydrodynamic effects and, therefore, rather independent on the irradiation wavelength.[108]

Using fused silica as an example, a model of thermo-convective transport based on the incompressible NSE was used to calculate possible periodicities that can emerge by the development of thermo-capillary instabilities in a horizontal liquid layer heated by fs-laser irradiation from the free-surface side.[67] Considering the temperature-dependent surface tension $\sigma(T)$ and viscosity $\mu(T)$, the growth rate γ of these instabilities was calculated as a function of the liquid molten layer thickness h and the mode periodicity Λ for $T = 2000$ K (**Figure 17**). The calculations predict an increase of the period of the fastest developing mode with increasing h allowing to explain both, sub- and supra-wavelength LIPSS experimentally observed on fused silica.[67,111] For relevant layer thicknesses, the calculated values of γ correspond to time durations $\gamma^{-1} \sim 10^{-12}$ to 10^{-10} s (i.e., 1–100 ps), which are smaller than melt lifetimes in the order of μs reported for fs-laser ablation of glasses.[119]

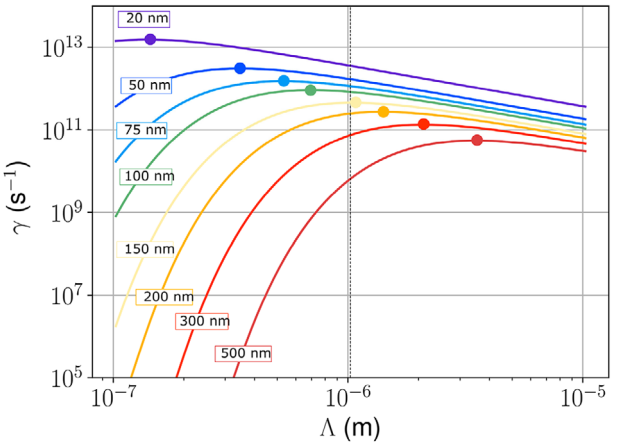

Figure 17. Growth rate γ of the thermo-convective instability as a function of the spatial period Λ of the unstable mode calculated for thin horizontal liquid layers of fused silica heated to $T = 2000$ K form the free-surface side by fs-laser irradiation. The dots identify the most unstable mode upon varying the layer thickness h from 20 to 500 nm. Reproduced under the terms of a Creative Commons BY 4.0 license.[67] Copyright 2018, The Authors, published by MDPI.

3.2.2. Self-Organization

The process of *self-organization* was first proposed in the 1990s to theoretically explain a specific class of periodic laser-induced structures that distinguished qualitatively from LIPSS as their orientation was unrelated to the polarization of the laser radiation and the structure period was not correlated directly to the exciting radiation wavelength.[120,121] The theory is based on the intensive laser-induced formation of nonequilibrium defects (e.g., interstitials, vacancies, voids, and dislocations) in a sub-surface layer of nm-thickness, in which a fluctuating local increase in defect concentration causes a corrugation of the surface relief and the corresponding surface strain (**Figure 18**).[122] Consequently, the structure formation was described as a result of laser-driven surface instabilities that develop due to the interaction of the defect concentration field with the self-consistent deformation of the elastic continuum of the host material. In this context, an important scaling parameter that determines the spatial periods of the corrugated surface topography was attributed to the thickness h of the defect-enriched near-surface layer.[122]

Later, the group around Reif and co-workers at the University of Cottbus, Germany, used the self-organization to describe the formation of LIPSS on wide bandgap materials such as BaF_2 and CaF_2 upon fs-laser irradiation.[123,124] The methodology was triggered mainly by the similarity of the experimentally observed structures with surface pattern induced by ion beam sputtering. Based on the detailed investigation of the interaction of high-power laser radiation with the aforementioned dielectric materials,[125] the generation and accumulation of local defects was also considered as a central aspect during structure formation.[126] According to this self-organization model, fs-laser irradiation initially leads to a rapid excitation of the electrons of the material during the pulse duration. The redistribution of this energy results in a softening of the atomic bonds and consequently in a destabilization of the crystal lattice in a thin surface layer (see Figure 3b). This disturbed system is in a highly unstable state, far away from thermodynamic equilibrium, whose degree of disturbance is further enhanced by the emission of individual components such as electrons, ions, atoms, and clusters. The time evolution of the growing surface profile is described by the competition of the elementary processes taking place in the sys-

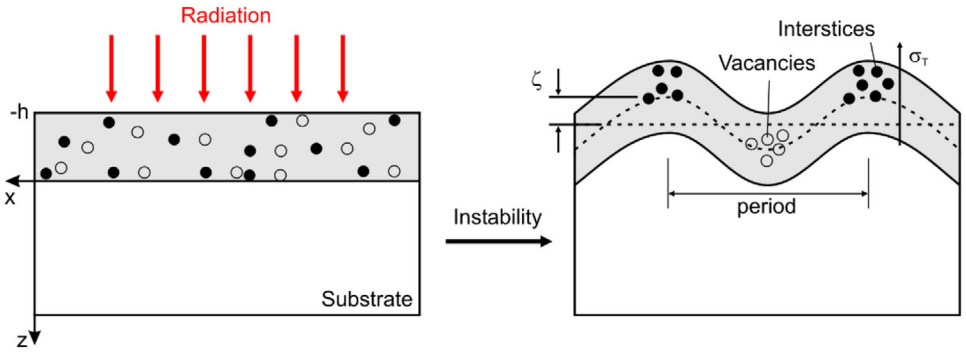

Figure 18. Formation of laser-induced periodic structures by self-organization: Laser irradiation results in the formation of point or extended defects in a sub-surface layer of thickness *h*. Diffusion and deformation-induced components in the deformed film lead to the accumulation of interstices (full circles) and vacancies (open circles) in regions of maximum tensile stress and maximum compressive stress, respectively. ζ represents the resulting displacement along *z* of the points of the central plane from their equilibrium position and is, therefore, a measure for the film strain. σ_T is the stress normal to the film surface. (Inspired by Figure 1 in Emel'yanov.[121])

tem: surface erosion (roughening) due to ablation and smoothing due to atomic diffusion and surface tension gradients.[126,127]

Mathematically, the model implements the temporal evolution of a growing surface profile $h(x,y,t)$[127]

$$\frac{\partial h}{\partial t} = -v(h)\sqrt{1+(\nabla h)^2} - D\Delta^2 h \tag{8}$$

The first term on the right-hand side describes surface erosion processes, with $v(h)$ being the surface curvature-dependent erosion velocity. The second term considers the thermal self-diffusion. The coefficient D depends on the activation energy for that process, the surface diffusivity, the surface density of diffusing atoms, and on the temperature.[127] With some additional simplifying assumptions on the (ion) erosion velocity, Equation (8) can be re-written as *anisotropic Kuramoto–Sivashinsky* type differential equation[128]—a prominent and well-studied description of many self-organization processes—that can be solved numerically. For additional details, the readers are referred to Valamova.[129]

This self-organization model was further developed in the following years by introducing the polarization dependence of the LIPSS formation process.[128] As one potential scenario, the asymmetry of the initial distribution of the kinetic energy of the electrons induced by the electric laser field was proposed, which leads to a corresponding asymmetric (polarization-dependent) energy transfer.

Figure 19 presents a comparison of experimentally observed LIPSS (upper row) and some numerical simulations (lower row) using the self-organization model upon irradiation with increasing dose.[130] Although a qualitative agreement of the surface morphologies was obtained, the authors noted that for the simulations no realistic scale could be provided as detailed material parameters are missing.

3.2.3. MD Simulations

MD simulations allow to model the laser interaction with solids with atomic resolution in three spatial dimensions and in time. In this approach developed during the 1950s, the trajectories of a set of interacting atoms are determined by numerically solving Newton's equations of motion.[131] The forces acting between the atoms and their potential energies are usually calculated by means of suitable empiric interatomic potentials. In this way, from a large ensemble of atoms macroscopic reorganization of matter based on microscopic interaction mechanisms can be tracked in time. Considering the computational resources typically required, MD simulations are nowadays limited to sizes of several hundreds of nanometers in all spatial dimensions and to simulated time spans up to several nanoseconds. If periodic boundary conditions can be assumed spatially, larger simulated dimensions can be realized. A crucial point in MD is the choice of interatomic potentials, which serve to compute the collective motion of all individual atoms. Time-independent potentials are often not suitable to consider the strong electronic excitation processes changing transiently the material properties upon high intensity laser irradiation particularly of semiconductors and dielectrics. Thus, they cannot properly account for rapid processes such as nonthermal or thermal melting occurring at fluences of the order of the ablation threshold, i.e., in the regime of LIPSS formation. In order to consider the transient changes in these materials, different interatomic potentials were calculated based on different microscopic electronic models, based on tight-binding theory[132] or by ab initio calculations using finite temperature density functional theory.[133] For metals, time-independent embedded atom models (EAMs) were used.[134]

In 2015, Ivanov et al.[135] presented the results of transient matter reorganization of a laser-irradiated bulk metal studied by TTM (see Section 3.1.5) coupled MD scheme (MD-TTM) based on an EAM interatomic potential. The authors implemented a 248 nm wavelength two-beam direct laser interference patterning scenario, where the interaction of a single 1.6 ps laser pulse with an Au target is simulated in air environment for time spans up to 500 ps. The two-beam interference imposed at the surface a sinusoidally modulated laser intensity pattern of 500 nm spatial period. The incident laser fluences were chosen below 0.4 J cm^{-2} near the damage threshold of the material, i.e., above the melting but below the threshold fluence of macroscopic ablation. Such a physical scenario can be considered as a basic

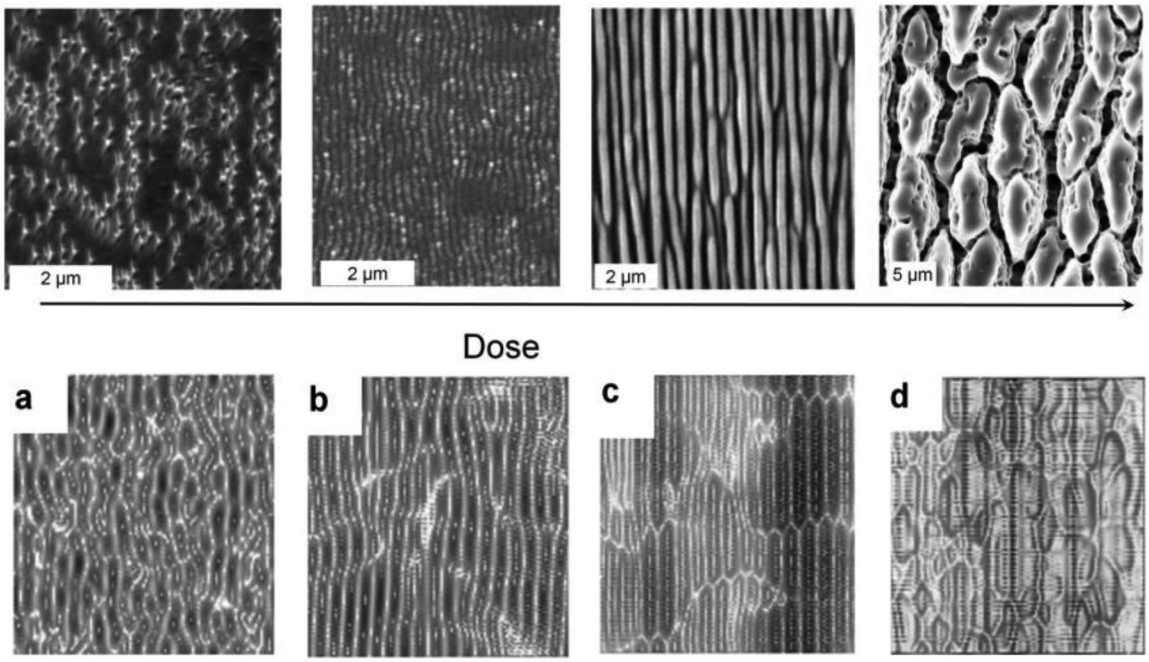

Figure 19. Comparison between SEM micrographs obtained from experimental investigations (upper row) with numerical simulation of self-organized pattern formation (lower row) as a function of irradiation dose. Note that for the simulation no realistic scale is given as detailed material parameters are missing. Reproduced with permission.[130] Copyright 2012, Elsevier.

approach to the early stage of LIPSS formation. Based on their simulations, the authors identified three competing mechanisms involved in the process of nanostructuring bulk Au targets by an ultrashort single UV laser pulse near the damage threshold: i) Under conditions of inertial stress confinement, the relaxation of laser-induced compressive stresses promotes the formation of sub-surface voids inside the molten part of the material at the areas with the highest incident energy. ii) The induced tensile stresses relax through the formation of voids. That relaxation establishes some hydrodynamic motion in the upper part of the liquid, finally resulting in the growth of surface structures. iii) Simultaneously, electron heat conduction into the bulk of the target causes strong cooling of the elevating surface structures and manifests in rapid surface solidification.

In 2017, the authors extended their MD-TTM simulations by implementing a comparison of the patterning of Au in air and with a 400 nm thick confining water layer both upon irradiation with single ultrashort laser pulses (400 fs duration, 248 nm wavelength) at maximum incident fluences between 0.16 and 0.25 J cm^{-2} distributed in 270 nm periodic beam patterns.[136] The results can be summarized as follows: the presence of a water confinement layer leads to a significant suppression of growing nanofeatures, finally resulting in a smoother structured surface when compared to irradiation in air. Due to the higher cooling rates, the water layer promotes a significantly faster solidification of the growing tip of the nanostructures. Moreover, at the given applied fluences, the formation of liquid metal droplets is suppressed in the water environment. Therefore, the resulting nanostructured surfaces are widely free of redeposited metal nanoparticles. The MD-TTM simulations of Shih et al. underlined the role of the Rayleigh–Taylor instability at the water/metal interface for the disintegration of the melt layer into nanoparticles for fs-laser irradiation of silver at higher laser fluences.[137]

Shugaev et al. employed a similar EAM interatomic potential-based MD-TTM simulation of the dynamics of single fs-laser pulse-induced phase transitions, material decomposition, and subsequent solidification of the metal Cr in air/vacuum triggered at fluences in the ablation regime.[112] Starting from a periodically modulated beam profile (of 260 nm lateral period, 200 fs pulse duration, 258 nm wavelength) with absorbed fluences ranging between 0.2 and 0.3 J cm^{-2} sufficient for phase explosion, spatially modulated ablation triggers a complex interplay of material removal and redistribution finally leading to the formation of surface features protruding above the original surface of the target. The authors pointed out that lateral pressure gradients in the ablation plume drive the vapor and liquid droplets of Cr toward the regions located above the minima of the laser energy deposition at the target surface. As a consequence of material redistribution, elongated liquid walls protruding up to ≈600 nm above the surface are transiently formed. The upper part of these liquid walls further disintegrates into nanoscale droplets, while the base of the wall solidifies within ≈2 ns, finally forming surface features of ≈100 nm height (see **Figure 20**). These MD simulations suggest that the redistribution of material from the lower lying part of the ablation plume plays a major role in the formation of the final surface protrusions. In contrast, the liquid flow in the molten regions of the sample that are subjected to the recoil pressure of the ablated material makes a minor contribution to the LIPSS formation only.

Later, the authors extended this work by considering water ambient environment during the fs-laser irradiation.[137,138] The laser-induced ablation plume was found to be rapidly decelerated

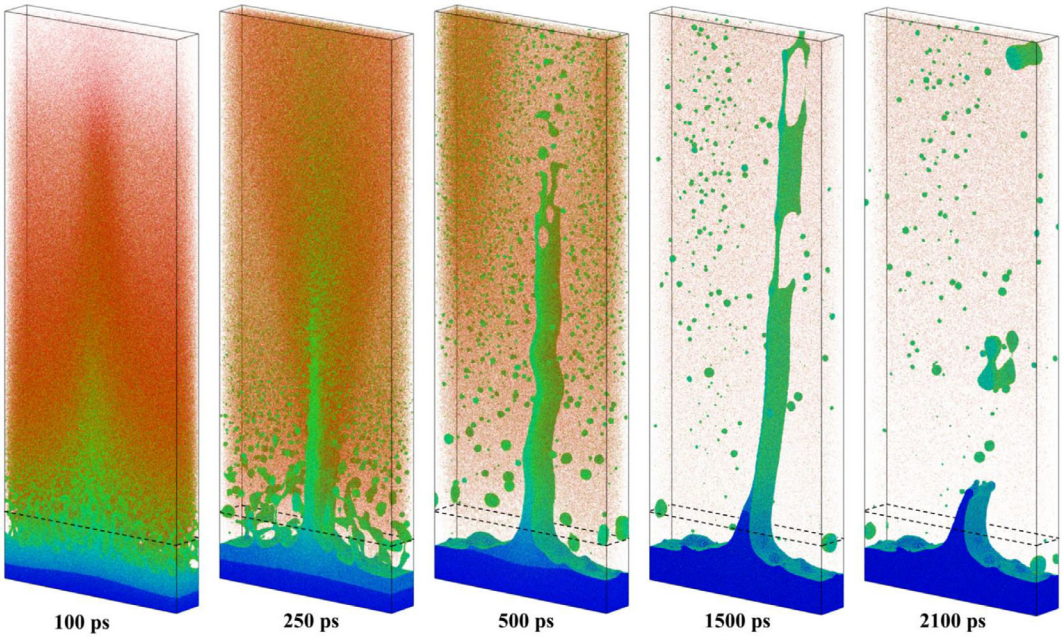

Figure 20. Sequence of atomistic snapshots obtained by MD-TTM simulations at different delay times after the single-pulse laser-excitation. The atoms are colored according to their potential energy indicating the solid phase as dark-blue, the liquid phase as light-blue, the free surface as green, and the vapor phase as red. Reproduced with permission.[112] Copyright 2017, American Physical Society.

and confined by the surrounding water, manifesting in the rapid disintegration of a hot metal layer formed at the interface between the ablation and water. Moreover, a large fraction of the ablation plume is laterally redistributed and then redeposited to the sample, finally resulting in smooth frozen surface features. In contrast to the spatial periods of LIPSS formed via ablation in air/vacuum, the geometrical dimensions and shape of the laser-induced surface features are less sensitive to the laser irradiation wavelength λ. These properties are largely determined by the thickness of the ablated layer and by the dynamics of the spatially confined interaction of the ablation plume with the water environment.[138]

4. Critical Assessment of LIPSS Theories

This section provides a critical assessment of the available LIPSS theories by adding a brief discussion of their weak points, common mistakes found in the literature (Sections 4.1 and 4.2), a comparison of their capabilities and performances (Section 4.3), and a clarification of the definition of relevant parameters and their relation to experiments (Section 4.4).

4.1. Assessment of Electromagnetic LIPSS Theories

In the following, several crucial points and common mistakes found in the literature referring to electromagnetic theories are provided:

- Variants of Equation (1), which do not correctly consider the complex-valued nature of the dielectric permittivities of the irradiated materials, are found in the LIPSS literature. These wrong variants may lead to incorrect values of the predicted spatial LIPSS periods. Moreover, Equation (1) does not answer the question, whether or not SPPs can be excited at the irradiated interface—a condition that is often ignored. For more details, the reader is referred to Raether[31] and Derrien et al.[32]
- Another common mistake arises from the fact that, via positive inter-pulse feedback, the spatial LIPSS period usually depends on the number of pulses applied per irradiated spot: many authors determined spatial LIPSS periods from multi-pulse experiments and then use Equation (1) to retrieve the (transient) dielectric permittivity of the irradiated material. However, this approach usually fails since for strong absorbing materials such as metals and semiconductors, the LIPSS period decreases by several tens of percent with increasing number of pulses per spot (see Figure 13). Hence, LIPSS periods determined from multi-pulse experiments should not be used for this single-pulse approach represented by Equation (1).
- Some authors proposed to use another variant of Equation (1), where $\Lambda_{\mathrm{LSFL}} = \Lambda_{\mathrm{SPP}}/2$, i.e., the modified model is predicting half of the LSFL period resulting from the "standard SPP model of LIPSS" discussed in Section 3.1.1. They justify this assumption by the formation of a standing plasmon wave that is created by two counter propagating SPPs. While this modified Equation (1) often seems to fit the experimentally determined LSFL periods better, the precise realization of that standing wave condition of anti-collinear SPPs excited at different and randomly distributed surface defects is still left open. Moreover, care must be taken here as well to avoid a comparison of single-pulse predictions with multi-pulse experiments (see the previous comment).

- Some additional limitations of the Sipe theory (see Section 3.1.2) should be mentioned here. The derivation of the analytical expressions behind Equation (4) is based on some mathematical linearizations through developments into Taylor series. This implies that the theory remains restricted to a near-surface layer, the so-called *selvedge region*. The extent l_S of that region has to fulfill two conditions.[18,72] First, the selvedge thickness must be small compared to the laser wavelength ($2\pi l_S/\lambda << 1$), and second, l_S must be small compared to the periodicity of the inhomogenous energy absorption ($|\boldsymbol{k}|l_S << 1$, with $\boldsymbol{k}$ being the LIPSS wave vector). The latter condition implies that HSFL may be too small to be properly described by the Sipe theory. Another particularity of Sipe's theory is that the surface roughness is implicitly encoded by two specific surface parameters, the shape factor *s* and the filling factor *F*, that cannot be easily adapted to pulse-to-pulse changes of the surface topography. So far, the latter has prevented that inter-pulse feedback through a changing surface roughness could be directly included in the Sipe theory.
- FDTD simulations are an extremely powerful approach to calculate the electromagnetic fields at almost arbitrary rough surfaces and to predict the resulting localized absorption of energy in the irradiated material underneath. A direct relation to physical effects, however, is often very difficult and requires a very careful analysis and interpretation of physical effects that may be involved. Moreover, numerical influences of spatial and temporal limitations must always be carefully checked.
- Under certain conditions, the electromagnetic scattering characteristics leading to the formation of LIPSS can be observed already in single-pulse irradiation experiments.[33,48,139] Often, this occurs at surface defects allowing an increased local absorption at local fluences close to the damage or ablation threshold of the irradiated materials. Some authors, however, report single-pulse LIPSS (LSFL-I) at very high fluences (up to 100 times the ablation threshold). Here, the presence of post-pulses or that of a temporally broad optical pulse pedestal (e.g., arising from amplified spontaneous emission) being capable to exceed the ablation threshold of the excited material must be carefully checked in the experiments. The same applies for the existence of pre-manufactured surface features (e.g., grinding grooves or scratches) that can seed the formation of periodic surface structures via optical scattering.[139]

4.2. Assessment of Matter Reorganization LIPSS Theories

In the following, several open questions found in the literature referring to matter reorganization theories are given:

- One of the most crucial and diversely discussed aspects is related to the experimentally proven relationship between the orientation of the LIPSS and the direction of the laser beam polarization.[15,80,81] Without the additional input of electromagnetic theories, most matter reorganization theories cannot convincingly explain the general coupling of the direction of LIPSS, which is usually either perpendicular or parallel to the laser beam polarization. Some of the matter reorganization theories may, however, explain certain observations of sub-wavelength or supra-wavelength LIPSS, which are formed in annular patterns or around the laser-irradiated spots and are not related to the laser polarization.[116]
- One of the prerequisites of forming LIPSS via matter reorganization is a sufficient long lifetime of the material surface in an excited state allowing for significant material transport. While this condition may be fulfilled for laser irradiation times (pulse durations) in the μs-range or even longer, it may not be valid for short (ns) or ultrashort (fs–ps) laser pulses. For semiconductors, the melt duration of the surface after fs-laser irradiation at fluences close to the ablation threshold typically ranges between a few and several tens of nanoseconds.[117,140] For metals (dielectrics), due to the higher (lower) heat conductivities, these durations are usually smaller (larger[119]).
- For hydrodynamic melt flows originating from the Marangoni effect, a simple estimate of the characteristic time scale required to transport some material over a radial distance L on a molten layer of average thickness h_m can be calculated via[119]

$$\tau_M \sim \frac{\mu L^2}{|\gamma_T| T_m h_m} \quad (9)$$

where μ is the dynamic viscosity of the melt, $|\gamma_T| = |d\gamma/dT|$ is the absolute value of the temperature coefficient of the surface tension γ, and T_m is the melting temperature of the material. When assuming as radial distance, the distance between neighbored maxima and minima of the "LSFL-modulated" surface temperature fields $L = \Lambda/2 \sim 400$ nm, an average melt depth of $h_m = 500$ nm, for silicon [$T_m = 1690$ K, $\mu = 0.9 \times 10^{-3}$ N s m^{-2}, $|\gamma_T| = 0.28 \times 10^{-3}$ N m^{-1} K^{-1}],[141] a characteristic time of Marangoni melt flow over a distance of half an LSFL period of $\tau_M \sim 1$ ns can be estimated. This time is of the order of experimentally reported melt durations. Note that the derivation of Equation (9) relies on a thin film approximation, where $h_m << L$ is assumed. While this condition can be fulfilled for the formation of LIPSS on metals, in semiconductors and dielectrics it may be violated. The latter is caused by the significantly larger melt depth that typically accounts to $h_m \sim 1$ μm in fs-laser-irradiated borosilicate glass.[119] In addition, glasses are subject to a specific transition from the solid to the vapor state during heating, which is why the viscosity μ of the melt changes over several orders of magnitude with increasing temperature. Consequently, for borosilicate glass with $|\gamma_T| = 3.4 \times 10^{-5}$ N m^{-1} K^{-1}, μ ($T = 1500$ K) $= 10^3$ N s m^{-2}, μ ($T > 2500$ K) = 1–10 N s m^{-2},[119] values of τ_M ranging between ms and μs are estimated using Equation (9). Based on the typical melt duration of $\approx$1 μs reported by Ben-Yakar et al.,[119] the strong temperature dependence of μ must therefore be considered when estimating the contribution of Marangoni convection to LSFL formation in a laser-induced molten glass layer.
- At first view, the manifold hydrodynamic effects and instabilities that were claimed to be relevant for LIPSS formation in Section 3.2.1 appear contradictive. However, it must be underlined here that the relevance and magnitude of hydrodynamic mechanisms can strongly vary among the different irradiated materials and the specific laser-irradiation conditions. Different analytical and numerical analyses are available addressing the relevance of various hydrodynamic instabilities under ultrashort laser pulse irradiation conditions.[108,142] On the basis of analytical estimations, Gurevich came to the

Table 2. Comparison of LIPSS theories concerning their capabilities and performances (meaning of symbols; (✓): yes; (×): no; (n.a.): not available at the current state; (-) not applicable for LIPSS).

LIPSS theory	Sipe	Sipe-Drude	SPP	FDTD	PIC	TTM	Hydro-/capillary models	Self-organization	MD
Analytical	✓	✓	✓	×	×	×	✓	✓	×
Numerical	×	×	×	✓	✓	✓	✓	✓	✓
Intra-pulse feedback	×	✓	✓	✓	✓	✓	×	×	×
Inter-pulse feedback	×	×	×	✓	n.a.	×	✓	✓	✓
2D	✓	✓	✓	✓	✓	✓	✓	✓	✓
3D	×	×	×	✓	n.a.	×	✓	×	✓
Surface	✓	✓	✓	✓	✓	✓	✓	✓	✓
Bulk	×	×	×	✓	✓	×	-	×	✓
Computing resources	low	low	low	high	high	medium	medium/high	medium	high
Commercial codes	×	×	×	✓	✓	×	×	×	×

conclusion that Rayleigh–Bénard convection and Marangoni effect, can be ruled out as origin of LIPSS on fs-laser-irradiated gold films, while recoil forces or the ablative Rayleigh–Taylor instability may contribute.[142] On the other hand, Rudenko et al. have convincingly demonstrated the relevance of the Marangoni instability as the origin of HSFL-II on fs-laser-irradiated Ni and steel through 3D-FDTD-coupled hydrodynamic simulations.[108] The authors stressed that the rather small Marangoni numbers estimated in the range of $Ma \sim 0.4$–2 (see Section 3.2.1) in this case cannot be used as a rigid criterion for the irrelevance of the Marangoni effect, where commonly values exceeding $Ma > 40$–80 are expected.[108] Moreover, these simulations did not evidence a direct influence of the Rayleigh–Taylor instability on HSFL-II. It must be concluded here that further work on the relevance of the hydrodynamic effects is required to clarify their relevance for other materials and irradiation conditions.

- Regarding the choice of compressible or incompressible NSE for hydrodynamic simulations, some comments should be provided here. The more general compressible NSE and the continuity equation according to Equations (6) and (7) along with the EOS are capable to describe the formation of pressure, shock, and rarefaction waves propagating in the irradiated material upon excitation at fluence close to the ablation threshold. The pressure and rarefaction waves were demonstrated to be essential for the destabilization of the laser-induced surface layer to trigger the formation of HSFL-II on metals via the Marangoni instability.[108] In contrast, shock/rarefaction waves cannot be described by an incompressible NSE model. Both NSE approaches can consider the recoil pressure as liquid layer destabilizing force for larger fluences and ablation rates.

4.3. Comparison of LIPSS Modeling Approaches: Capabilities and Performances

Table 2 provides a systematic comparison of the different LIPSS modeling approaches regarding their capabilities and the numerical performances (costs) required. Ticks and crosses indicate whether the corresponding properties are given or not. The necessary computing resources indicate the numerical costs of the different approaches. Approaches that must be treated numerically for studying LIPSS (e.g., due to their description by nonlinear partial differential equations) are termed "numerical." If a direct algebraic evaluation is possible, they are considered as "analytical" here.

4.4. Assessment of Key Parameters: Comparison with Experiments

It is known from a large amount of available experimental LIPSS studies that for each material their formation and appearance depend crucially on several key parameters, such as irradiation wavelength, polarization, fluence, number of pulses, angle of incidence, and the ambient environment.[13,15,143] Most of these parameters were already introduced and discussed in Section 3. Some of these parameters are rather easy to determine and control, while others must be carefully analyzed to allow a relation with theories. The following part sheds some light on aspects that should be considered when comparing theoretical and experimental results on LIPSS. That includes particularly the usage of different definitions of key laser and processing parameters, such as the terms intensity/fluence, the number of (effective) pulses, and their relation to distinct threshold fluences.

- Energy deposition is the key in the formation of LIPSS. While some publications in the context of LIPSS just specify the measured laser *pulse energy* (E, in [J]), a more meaningful parameter is the single-pulse laser *fluence* [J cm^{-2}, areal energy density] incident to the surface, as it already considers the laser beam focusing conditions. Some authors alternatively specify the *intensity* [W cm^{-2}, areal power density] of a single laser pulse. Often LIPSS do not strongly depend on the laser pulse duration and the fluences can be straightforwardly calculated from the pulse intensity as its product with pulse duration (with some correction factors close to unity). Since real laser sources usually emit spatially Gaussian laser beams without a sharp boundary, it must be specified whether the *peak fluence* (ϕ_0) or the *average fluence* ($\phi = \phi_0/2$) are used (the same for intensities). Moreover, since Gaussian beams are relying

on some particular definitions, it must be specified whether the laser beam waist radius (w_0) at the sample surface refers to the $1/e$- or the $1/e^2$-decay length of the spatial intensity/fluence profile. This choice then determines whether $\phi_0 = E/(\pi\ {w_0}^2)$, or $\phi_0 = 2E/(\pi\ {w_0}^2)$ should be used for the calculation of the peak fluence from the experimentally measured pulse energy.

- In simulations of LIPSS often *absorbed fluences* are used, which can be calculated from the incident fluences via considering the losses imposed by the reflection of the incident radiation at the surface/interfaces of the solid. In the linear interaction regime and as first approximation, this is mediated via the *Fresnel reflectivity* (R) that depends on the wavelength, angle of incidence, and polarization state. For nonlinear interactions, intrapulse changes of the surface reflectivity may be considered that are caused by transient changes of the material-specific dielectric permittivity (ϵ).
- Some authors use the term *accumulated fluences* ([J cm^{-2}], sometimes referred to as *dose*) as the product between the (peak) fluence per pulse and the number of applied pulses ($\phi_{acc} = \phi_0 \times N$). However, while this reduces the number of specified parameters, this parameter must be taken with care since material-specific thresholds are involved in LIPSS formation (see below). Just to illustrate the problem of this oversimplification here: the surface morphologies caused by a certain number of laser pulses at a fluence, e.g., one to two times the threshold for twice the number of pulses, are very different from that obtained at twice that number of pulses at half the fluence, i.e., below the threshold.
- The generation of LIPSS with a spatially varying fluence profile $\phi(x,y)$ results in other aspects that must be considered with care. LIPSS are usually a multi-pulse phenomenon, where inter-pulse feedback plays an important role (as already discussed above). For the irradiation of a single spot at the surface by N consecutive laser pulses, each location is hit N-times with the identical fluence value. As a consequence, distinct, spatially separated surface regions covered by different types of LIPSS (HSL, LSFL, grooves, etc.) can be distinguished. This situation is physically different from what is realized upon scan-processing of 1D lines, that are typically performed at a constant scan velocity (v_x, e.g., in the x-direction) within a line. 2D areas can be processed by meandering displacement of such lines in the orthogonal y-direction (at a selected offset Δy). Here, for line-scanning with a nonzero pulse-to-pulse spot overlap ($0 < \Delta x < 2w_0$), a fixed location at the surface is first exposed to a reduced local laser fluence from the rising edge of the discretely displaced spatially Gaussian laser beam profile, before further increased fluence values from the most intense part and finally from the falling edge of the laser beam profile hit the specific location (depending on the value of Δx). If 2D areas with nonzero line-overlap ($0 < \Delta y < 2w_0$) are processed, additional exposures manifest at the selected surface location through the scanning of multiple overlapping lines (depending on the value of Δy). In such a scanning approach, surface structures formed in the high fluence part of the scanned laser-beam can later be "overwritten" by the low fluence tail of the Gaussian beam profile, often resulting in hierarchical micro-nano-structures with different types of LIPSS being superimposed.[143] To at least roughly allow for some inter-comparison of spot, line, and area processing with a pulsed laser beam (repetition frequency (f_{rep})), the concept of *effective number of laser pulses* per beam spot area is often used[144,145]

$$N_{eff,1D} = \frac{2w_0}{\Delta x} = \frac{2w_0 \cdot f_{rep}}{v_x} \tag{10}$$

$$N_{eff,2D} = \frac{\pi w_0^2 \cdot f_{rep}}{v_x \cdot \Delta y} \tag{11}$$

However, it is important to underline that N, $N_{eff,1D}$, and $N_{eff,2D}$ cannot simply be considered as "the same parameter considering the number of laser pulse exposures." None of the available microscopic LIPSS theories includes such laser beam scanning effects, although the theoretical approaches of Eichstädt et al.[146] and Mezera et al.[147] based on accumulated fluences can be used to empirically predict experimental parameter ranges for processing of homogenous areas of LIPSS.

- Regardless the laser processing strategy, it is an experimental fact that LIPSS are most pronounced in specific fluence and pulse number ranges. These regimes strongly depend on the irradiated materials and are usually associated with certain material-specific modification thresholds, such as the fluence thresholds of melting or ablation that are usually associated with phase transitions in the irradiated material. In dielectrics, nonlinear absorption/ionization phenomena driving the conduction band electron density above a critical value impose a threshold. Sometimes other crucial parameters such as the chemical bond energy of organic polymers were identified.[148] It is essential to note that the same physical mechanisms leading to periodic energy localization (such as, e.g., the excitation of SEWs/SPPs and the interference of their electromagnetic field with the incident laser radiation) can even result in different manifestations of the LIPSS: while in the ablative regime, a periodic surface topography relief (LSFL-I) is formed through localized material removal,[33] at lower fluences in the melting regime, the rapid resolidification of the locally molten material can induce structural changes, such as amorphization, leaving behind an almost flat surface with a strong periodic modulation of the optical surface reflectivity.[26,33]

5. Outlook

After more than five decades of research on LIPSS, including an ongoing revival of the research interest at the turn of the millennium, the current status of knowledge can be summarized as follows: The "battle"/competition of the different LIPSS theories (*electromagnetics* vs *matter reorganization*) is almost over. Both theoretical approaches are currently merging into a coherent view on these surface nanostructures, where, depending on the materials and irradiation conditions, aspects supporting one of the two theory classes can dominate the experimental observations. While in most cases, the LIPSS characteristics are seeded through different excitation/absorption channels in an ultrafast manner already during the irradiation via electromagnetic scattering and interference effects at the rough surface, relevant hydrodynamic motions and diffusion effects may contribute on longer timescales up to the ms-range (depending

on the materials). In that sense, and as implied by the title of this review article, "Maxwell meets Marangoni" in an abstracted way—although it is not known to the authors whether *James Clerk Maxwell* (* 13 June 1831 in Edinburgh; † 5 November 1879 in Cambridge) and *Carlo Giuseppe Matteo Marangoni* (* 29 April 1840 in Pavia; † 14 April 1925 in Florence) have ever had the opportunity to interact in person.

This unified view on LIPSS became possible, among other things, by ultrafast time-resolved experiments and the development of multi-physical simulations considering and connecting both classes of theories on complementing spatio-temporal scales. Apart from the significantly improved theoretical understanding developed during the past years, one can also observe an ongoing practical interest in LIPSS, e.g., for adding specific tailor-made functionalities to surfaces with processing rates of up to $m^2\ s^{-1}$ to meet the demands of current industrial applications. These experimental efforts were recently reviewed by the authors elsewhere.[13,143] An ongoing research line is currently exploring the role of chemical effects that are involved in the formation of LIPSS. Most of the current theories are not capable to include these effects. Among the available approaches, MD simulations may offer relevant contributions in the future, as they can track large ensembles of individual atoms/molecules and could be coupled with FDTD calculations.

Conflict of Interest

The authors declare no conflict of interest.

Acknowledgements

Open access funding enabled and organized by Projekt DEAL.

Keywords

electromagnetic theories, hydrodynamic, laser-induced periodic surface structures (LIPSS), matter reorganization theories, self-organization, surface plasmon polaritons

Received: May 18, 2020
Revised: July 6, 2020
Published online: August 31, 2020

[1] M. Birnbaum, *J. Appl. Phys.* **1965**, *36*, 3688.
[2] J. Heitz, E. Ahrenholz, D. Bäuerle, R. Sauerbrey, H. M. Phillips, *Appl. Phys. A* **1994**, *59*, 289.
[3] J. Bonse, S. Höhm, M. Hartelt, D. Spaltmann, S. Pentzien, R. Koter, S. Marschner, A. Rosenfeld, J. Krüger, in *Optically Induced Nanostructures* (Eds: K. König, A. Ostendorf), Walther De Gruyter, Berlin, Germany **2015**, Ch. 7.
[4] S. Höhm, A. Rosenfeld, J. Krüger, J. Bonse, *Appl. Phys. Lett.* **2013**, *102*, 054102.
[5] J. Bonse, J. Krüger, S. Höhm, A. Rosenfeld, *J. Laser Appl.* **2012**, *24*, 042006.
[6] R. Buividas, M. Mikutis, S. Juodkazis, *Prog. Quantum Electron.* **2014**, *38*, 119.
[7] T.-H. Her, in *Comprehensive Nanoscience and Technology, Vol. 4: Nanofabrication and Devices*, (Eds: D. Andrews, G. Scholes, G. Wiederrecht), Ch. 10, pp. 277–314, Academic Press, New York **2011**.
[8] A. Y. Vorobyev, C. Guo, *Laser Photonics Rev.* **2013**, *7*, 385.
[9] F. Müller, C. Kunz, S. Gräf, *Materials* **2016**, *9*, 476.
[10] J. Bonse, S. V. Kirner, M. Griepentrog, D. Spaltmann, J. Krüger, *Materials* **2018**, *11*, 801.
[11] H. Liu, W. Lin, M. Hong, *APL Photonics* **2019**, *4*, 051101.
[12] C. Florian, S. V. Kirner, J. Krüger, J. Bonse, *J. Laser Appl.* **2020**, *32*, 022063.
[13] S. Gräf, *Adv. Opt. Technol.* **2020**, *9*, 11.
[14] E. Stratakis, J. Bonse, J. Heitz, J. Siegel, G. D. Tsibidis, E. Skoulas, A. Papadopoulos, A. Mimidis, A. C. Joel, P. Comanns, J. Krüger, C. Florian, Y. Fuentes-Edfuf, J. Solis, W. Baumgartner, *Mater. Sci. Eng., R* **2020**, *141*, 100562.
[15] J. Bonse, S. Höhm, S. V. Kirner, A. Rosenfeld, J. Krüger, *IEEE J. Sel. Top. Quantum Electron.* **2017**, *23*, 9000615.
[16] H. M. van Driel, J. E. Sipe, J. F. Young, *Phys. Rev. Lett.* **1982**, *49*, 1955.
[17] Z. Guosheng, P. M. Fauchet, A. E. Siegman, *Phys. Rev. B* **1982**, *26*, 5366.
[18] J. E. Sipe, J. F. Young, J. S. Preston, H. M. van Driel, *Phys. Rev. B* **1983**, *27*, 1141.
[19] J. F. Young, J. S. Preston, H. M. van Driel, J. E. Sipe, *Phys. Rev. B* **1983**, *27*, 1155.
[20] J. F. Young, J. E. Sipe, H. M. van Driel, *Phys. Rev. B* **1984**, *30*, 2001.
[21] H. M. van Driel, J. E. Sipe, J. F. Young, *J. Lumin.* **1985**, *30*, 446.
[22] A. E. Siegman, P. M. Fauchet, *IEEE J. Quantum Electron.* **1986**, *22*, 1384.
[23] O. Varlamova, J. Reif, *J. Laser Micro/Nanoeng.* **2013**, *8*, 300.
[24] K. Sokolowski-Tinten, A. Barty, S. Boutet, U. Shymanovich, H. Chapman, M. Bogan, S. Marchesini, S. Hau-Riege, N. Stojanovic, J. Bonse, Y. Rosandi, H. M. Urbassek, R. Tobey, H. Ehrke, A. Cavalleri, S. Düsterer, H. Redlin, M. Frank, S. Bajt, J. Schulz, M. Seibert, J. Hajdu, R. Treusch, C. Bostedt, M. Hoener, T. Möller, *AIP Conf. Proc.* **2010**, *1278*, 373.
[25] S. Höhm, M. Herzlieb, A. Rosenfeld, J. Krüger, J. Bonse, *Appl. Surf. Sci.* **2016**, *374*, 331.
[26] M. Garcia-Lechuga, D. Puerto, Y. Fuentes-Edfuf, J. Solis, J. Siegel, *ACS Photonics* **2016**, *3*, 1961.
[27] S. A. Akhmanov, V. I. Emel'yanov, N. I. Koroteev, V. N. Seminogov, *Sov. Phys. Usp.* **1985**, *28*, 1084.
[28] P. A. Temple, M. J. Soileau, *IEEE J. Quantum Electron.* **1981**, *17*, 2067.
[29] A. M. Bonch-Bruevich, M. N. Libenson, V. S. Makin, V. V. Trubaev, *Opt. Eng.* **1992**, *31*, 718.
[30] F. Keilmann, Y. H. Bai, *Appl. Phys. A* **1982**, *29*, 9.
[31] H. Raether, *Surface Plasmons on Smooth and Rough Surfaces and on Gratings*, Springer-Verlag, Berlin, Germany **1988**.
[32] T. J.-Y. Derrien, J. Krüger, J. Bonse, *J. Opt.* **2016**, *18*, 115007.
[33] J. Bonse, A. Rosenfeld, J. Krüger, *J. Appl. Phys.* **2009**, *106*, 104910.
[34] M. Huang, F. Zhao, Y. Cheng, N. Xu, Z. Xu, *ACS Nano* **2009**, *3*, 4062.
[35] M. J. Abere, M. Zhong, J. Krüger, J. Bonse, *MRS Bull.* **2016**, *41*, 969.
[36] F. Garrelie, J. P. Colombier, F. Pigeon, S. Tonchev, N. Faure, M. Bounhalli, S. Reynaud, O. Parriaux, *Opt. Express* **2011**, *19*, 9035.
[37] W. L. Barnes, A. Dereux, T. W. Ebbesen, *Nature* **2003**, *424*, 824.
[38] N. Rotenberg, J. E. Sipe, *Phys. Rev. B* **2011**, *83*, 045416.
[39] G. Miyaji, K. Miyazaki, *Opt. Express* **2008**, *16*, 16265.
[40] M. Straub, M. Afshar, D. Feili, H. Seidel, K. König, *J. Appl. Phys.* **2012**, *111*, 124315.
[41] E. V. Golosov, A. A. Ionin, Y. R. Kolobov, S. I. Kudryashov, A. E. Ligachev, S. V. Makarov, Y. N. Novoselov, L. V. Seleznev, D. V. Sinitsyn, A. R. Sharipov, *Phys. Rev. B* **2011**, *83*, 115426.
[42] E. V. Golosov, A. A. Ionin, Y. R. Kolobov, S. I. Kudryashov, A. E. Ligachev, Y. N. Novoselov, L. V. Seleznev, D. V. Sinitsyn, *J. Exp. Theor. Phys.* **2011**, *113*, 14.

[43] T. J.-Y. Derrien, R. Koter, J. Krüger, S. Höhm, A. Rosenfeld, J. Bonse, *J. Appl. Phys.* **2014**, *116*, 074902.
[44] A. V. Dostovalov, T. J.-Y. Derrien, S. A. Lizunov, F. Přeučil, K. A. Okotrub, T. Mocek, V. P. Korolkov, S. A. Babin, N. M. Bulgakova, *Appl. Surf. Sci.* **2019**, *491*, 650.
[45] J. E. Sipe, H. M. van Driel, J. F. Young, *Can. J. Phys.* **1985**, *63*, 104.
[46] A. Rudenko, J.-P. Colombier, S. Höhm, A. Rosenfeld, J. Krüger, J. Bonse, T. E. Itina, *Sci. Rep.* **2017**, *7*, 12306.
[47] A. Rudenko, C. Mauclair, F. Garrelie, R. Stoian, J.-P. Colombier, *Nanophotonics* **2019**, *8*, 459.
[48] D. C. Emmony, R. P. Howson, L. J. Willis, *Appl. Phys. Lett.* **1973**, *23*, 598.
[49] T. Y. Hwang, C. Guo, *J. Appl. Phys.* **2010**, *108*, 073523.
[50] J. C. Maxwell Garnett, *Philos. Trans. R. Soc. London, Ser. A* **1904**, *203*, 385.
[51] A. Abdelmalek, B. Sotillo, Z. Bedrane, V. Bharadwaj, S. Pietralunga, R. Ramponi, E.-H. Amara, S. M. Eaton, *AIP Adv.* **2017**, *7*, 105105.
[52] L. Wang, Q.-D. Chen, X.-W. Cao, R. Buividas, X. Wang, S. Juodkazis, H.-B. Sun, *Light: Sci. Appl.* **2017**, *6*, e17112.
[53] G. Miyaji, M. Hagiya, K. Miyazaki, *Phys. Rev. B* **2017**, *96*, 045122.
[54] H. Iwase, S. Kokubo, S. Juodkazis, H. Misawa, *Opt. Express* **2009**, *17*, 4388.
[55] S. N. Volkov, A. E. Kaplan, K. Miyazaki, *Appl. Phys. Lett.* **2009**, *94*, 041104.
[56] J. Bonse, M. Munz, H. Sturm, *J. Appl. Phys.* **2005**, *97*, 013538.
[57] S. Baudach, J. Bonse, W. Kautek, *Appl. Phys. A* **1999**, *69*, S395.
[58] J. Reif, F. Costache, M. Henyk, S. V. Pandelov, *Appl. Surf. Sci.* **2002**, *197–198*, 891.
[59] F. Costache, *Ph.D. Thesis*, Brandenburgische Technische Universität Cottbus, Germany **2006**.
[60] M. Zhou, H. F. Yang, B. J. Li, J. Dai, J. K. Di, E. L. Zhao, L. Cai, *Appl. Phys. A* **2009**, *94*, 571.
[61] S. Höhm, A. Rosenfeld, J. Krüger, J. Bonse, *J. Appl. Phys.* **2012**, *112*, 014901.
[62] D. Dufft, A. Rosenfeld, S. K. Das, R. Grunwald, J. Bonse, *J. Appl. Phys.* **2009**, *105*, 034908.
[63] H. Zhang, J.-P. Colombier, S. Witte, *Phys. Rev. B* **2020**, *101*, 245430.
[64] S. He, J. J. J. Nivas, A. Vecchione, M. Hu, S. Amoruso, *Opt. Express* **2016**, *24*, 3238.
[65] D. R. Austin, K. R. P. Kafka, Y. H. Lai, Z. Wang, K. Zhang, H. Li, C. I. Blaga, A. Y. Yi, L. F. DiMauro, E. A. Chowdhury, *J. Appl. Phys.* **2016**, *120*, 143103.
[66] S. Gräf, C. Kunz, F. Müller, *Materials* **2017**, *10*, 933.
[67] S. Gräf, C. Kunz, S. Engel, T. J.-Y. Derrien, F. Müller, *Materials* **2018**, *11*, 1340.
[68] C. Kunz, T. N. Büttner, B. Naumann, A. V. Boehm, E. Gnecco, J. Bonse, C. Neumann, A. Turchanin, F. A. Müller, S. Gräf, *Carbon* **2018**, *133*, 176.
[69] L. Museur, G. D. Tsibidis, A. Manousaki, D. Anglos, A. Kanaev, *J. Opt. Soc. Am. B* **2018**, *35*, 2600.
[70] G. Deng, Y. Xiao, M. Yang, H. Zhou, H. Yang, G. Feng, S. Zhou, *Laser Phys. Lett.* **2019**, *16*, 056007.
[71] K. Yee, *IEEE Trans. Antennas Propag.* **1966**, *14*, 302.
[72] J. Z. P. Skolski, G. R. B. E. Römer, J. V. Obona, V. Ocelik, A. J. Huis in 't Veld, J. T. M. De Hosson, *Phys. Rev. B* **2012**, *85*, 075320.
[73] J. Z. P. Skolski, G. R. B. E. Römer, J. V. Obona, A. J. Huis in't Veld, *J. Appl. Phys.* **2014**, *115*, 103102.
[74] J.-L. Déziel, J. Dumont, D. Gagnon, L. J. Dubé, S. H. Messaddeq, Y. Messaddeq, *J. Opt.* **2015**, *17*, 075405.
[75] J. Z. P. Skolski, G. R. B. E. Römer, J. V. Obona, V. Ocelik, A. J. Huis in't Veld, J. T. M. De Hosson, *J. Laser Micro/Nanoeng.* **2013**, *8*, 1.
[76] H. Zhang, J.-P. Colombier, C. Li, N. Faure, G. Cheng, R. Stoian, *Phys. Rev. B* **2015**, *92*, 174109.
[77] J.-L. Déziel, J. Dumont, D. Gagnon, L. J. Dubé, S. H. Messaddeq, Y. Messaddeq, *Phys. Status Solidi C* **2016**, *13*, 121.
[78] M. Huang, Y. Cheng, F. Zhao, Z. Xu, *Ann. Phys.* **2013**, *525*, 74.
[79] S. Hou, Y. Huo, P. Xiong, Y. Zhang, S. Zhang, T. Jia, Z. Sun, J. Qiu, Z. Xu, *J. Phys. D: Appl. Phys.* **2011**, *44*, 505401.
[80] S. Gräf, F. A. Müller, *Appl. Surf. Sci.* **2015**, *331*, 150.
[81] J. J. J. Nivas, S. He, A. Rubano, A. Vecchione, D. Paparo, L. Marrucci, R. Bruzzese, S. Amoruso, *Sci. Rep.* **2015**, *5*, 17929.
[82] N. Livakas, E. Skoulas, E. Stratakis, *Opto-Electron. Adv.* **2020**, *3*, 190035.
[83] Y. Shen, X. Wang, Z. Xie, C. Min, X. Fu, Q. Liu, M. Gong, X. Yuan, *Light: Sci. Appl.* **2019**, *8*, 90.
[84] Y. Shimotsuma, P. G. Kazansky, J. Qiu, K. Hirao, *Phys. Rev. Lett.* **2003**, *91*, 247405.
[85] V. R. Bhardwaj, E. Simova, P. P. Rajeev, C. Hnatovsky, R. S. Taylor, D. M. Rayner, P. B. Corkum, *Phys. Rev. Lett.* **2006**, *96*, 057404.
[86] R. Buschlinger, S. Nolte, U. Peschel, *Phys. Rev. B* **2014**, *89*, 184306.
[87] M. Hörstmann-Jungemann, J. Gottmann, D. Wortmann, *J. Laser Micro/Nanoeng.* **2009**, *4*, 135.
[88] R. Buividas, L. Rosa, R. Sliupas, T. Kudrius, G. Slekys, V. Datsyuk, S. Juodkazis, *Nanotechnology* **2011**, *22*, 055304.
[89] A. Rudenko, C. Mauclair, F. Garrelie, R. Stoian, J.-P. Colombier, *Appl. Surf. Sci.* **2019**, *470*, 228.
[90] M. Mezera, J. Bonse, G. R. B. E. Römer, *Polymers* **2019**, *11*, 1947.
[91] A. Rudenko, C. Mauclair, F. Garrelie, R. Stoian, J.-P. Colombier, *Phys. Rev. B* **2019**, *99*, 235412.
[92] G. D. Tsibidis, A. Mimidis, E. Skoulas, S. V. Kirner, J. Krüger, J. Bonse, E. Stratakis, *Appl. Phys. A* **2018**, *124*, 27.
[93] J. Bonse, J. Krüger, *J. Appl. Phys.* **2010**, *108*, 034903.
[94] J. Bonse, S. Höhm, A. Rosenfeld, J. Krüger, *Appl. Phys. A* **2013**, *110*, 547.
[95] C. Florian, J.-L. Déziel, S. V. Kirner, J. Siegel, J. Bonse, *Nanomaterials* **2020**, *10*, 147.
[96] F. H. Harlow, Los Alamos Scientific Laboratory Report LAMS-1956, Los Alamos Scientific Laboratory, Los Alamos, NM **1955**.
[97] Wikipedia encyclopedia entry "Particle-in-cell"; https://en.wikipedia.org/wiki/Particle-in-cell (accessed: June 2020).
[98] M. Djouder, T. E. Itina, D. Deghiche, O. Lamrous, *Appl. Surf. Sci.* **2012**, *258*, 2580.
[99] M. Djouder, O. Lamrous, M. D. Mitiche, T. E. Itina, M. Zemirli, *Appl. Surf. Sci.* **2013**, *280*, 711.
[100] A. M. Gouda, H. Sakagami, T. Ogata, M. Hashida, S. Sakabe, *Plasma Fusion Res.* **2016**, *11*, 2401071.
[101] A. M. Gouda, *Ph.D. Thesis*, Nagoya University, Japan **2018**.
[102] A. Russel, *Ph.D. Thesis*, Ohio State University, USA **2019**.
[103] T. J.-Y. Derrien, T. Sarnet, M. Sentis, T. E. Itina, *J. Optoelectron. Adv. Mater.* **2010**, *12*, 610.
[104] S. I. Anisimov, B. L. Kapeliovich, T. L. Perel'man, *Sov. Phys. Technol. Phys.* **1974**, *39*, 375.
[105] E. L. Gurevich, Y. Levy, S. V. Gurevich, N. M. Bulgakova, *Phys. Rev. B* **2017**, *95*, 054305.
[106] Y. Levy, T. J.-Y. Derrien, N. M. Bulgakova, E. L. Gurevich, T. Mocek, *Appl. Surf. Sci.* **2016**, *374*, 157.
[107] A. Rudenko, *Ph.D. Thesis*, Jean Monnet University, Saint-Étienne, France **2017**.
[108] A. Rudenko, A. Abou-Saleh, F. Pigeon, C. Mauclair, F. Garrelie, R. Stoian, J.-P. Colombier, *Acta Mater.* **2020**, *194*, 93.
[109] G. D. Tsibidis, M. Barberoglou, P. A. Loukakos, E. Stratakis, C. Fotakis, *Phys. Rev. B* **2012**, *86*, 115316.
[110] G. D. Tsibidis, E. Stratakis, K. E. Aifantis, *J. Appl. Phys.* **2012**, *111*, 053502.
[111] G. D. Tsibidis, E. Skoulas, A. Papadopoulos, E. Stratakis, *Phys. Rev. B* **2016**, *94*, 081305.

[112] M. V. Shugaev, I. Gnilitskyi, N. M. Bulgakova, L. V. Zhigilei, *Phys. Rev. B* **2017**, *96*, 205429.
[113] T. R. Anthony, H. E. Cline, *J. Appl. Phys.* **1977**, *48*, 3888.
[114] D. Jost, W. Lüthy, H. P. Weber, R. P. Salanthé, *Appl. Phys. Lett.* **1986**, *49*, 625.
[115] V. I. Emel'yanov, I. F. Uvarova, *Izv. Akad. Nauk SSSR, Ser. Fiz.* **1986**, *50*, 1214.
[116] G. Gorodetsky, J. Kanicki, T. Kazyaka, R. L. Melcher, *Appl. Phys. Lett.* **1985**, *46*, 547.
[117] D. von der Linde, K. Sokolowski-Tinten, *Appl. Surf. Sci.* **2000**, *154–155*, 1.
[118] G. D. Tsibidis, C. Fotakis, E. Stratakis, *Phys. Rev. B* **2015**, *92*, 041405(R).
[119] A. Ben-Yakar, A. Harkin, J. Ashmore, R. L. Byer, H. A. Stone, *J. Phys. D: Appl. Phys.* **2007**, *40*, 1447.
[120] V. I. Emel'yanov, *Laser Phys.* **1992**, *2*, 389.
[121] V. I. Emel'yanov, *Quantum Electron.* **1999**, *29*, 561.
[122] V. I. Emel'yanov, *Laser Phys.* **2008**, *18*, 682.
[123] F. Costache, M. Henyk, J. Reif, *Appl. Surf. Sci.* **2002**, *186*, 352.
[124] F. Costache, M. Henyk, J. Reif, *Appl. Surf. Sci.* **2003**, *208–209*, 486.
[125] J. Reif, *Opt. Eng.* **1989**, *28*, 1122.
[126] J. Reif, F. Costache, M. Bestehorn, in *Recent Advances in Laser Processing of Materials* (Eds: J. Perriere, E. Millon, E. Fogarassy), Elsevier, Amsterdam, Netherlands **2006**, Ch. 9.
[127] O. Varlamova, F. Costache, J. Reif, M. Bestehorn, *Appl. Surf. Sci.* **2006**, *252*, 4702.
[128] J. Reif, O. Varlamova, S. Varlamov, M. Bestehorn, *Appl. Phys. A* **2011**, *104*, 969.
[129] O. Varlamova, *Ph.D. Thesis*, Brandenburgische Technische Universität Cottbus, Germany **2013**.
[130] O. Varlamova, M. Bounhalli, J. Reif, *Appl. Surf. Sci.* **2013**, *278*, 62.
[131] B. J. Alder, T. E. Wainwright, *J. Chem. Phys.* **1959**, *31*, 459.
[132] H. O. Jeschke, M. E. Garcia, M. Lenzner, J. Bonse, J. Krüger, W. Kautek, *Appl. Surf. Sci.* **2002**, *197–198*, 839.
[133] P. L. Silvestrelli, A. Alavi, M. Parrinello, D. Frenkel, *Phys. Rev. Lett.* **1996**, *77*, 3149.
[134] V. V. Zhakhovskii, N. A. Inogamov, Y. V. Petrov, S. I. Ashitkov, K. Nishihara, *Appl. Surf. Sci.* **2009**, *255*, 9592.
[135] D. S. Ivanov, V. P. Lipp, A. Blumenstein, F. Kleinwort, V. P. Veiko, E. Yakovlev, V. Roddatis, M. E. Garcia, B. Rethfeld, J. Ihlemann, P. Simon, *Phys. Rev. Appl.* **2015**, *4*, 064006.
[136] D. S. Ivanov, A. Blumenstein, J. Ihlemann, P. Simon, M. E. Garcia, B. Rethfeld, *Appl. Phys. A* **2017**, *123*, 744.
[137] C.-Y. Shih, M. V. Shugaev, C. Wu, L. V. Zhigilei, *J. Phys. Chem. C* **2017**, *121*, 16549.
[138] C.-Y. Shih, I. Gnilitskyi, M. V. Shugaev, E. Skoulas, E. Stratakis, L. V. Zhigilei, *Nanoscale* **2020**, *12*, 7674.
[139] M. J. Soileau, *IEEE J. Quantum Electron.* **1984**, *20*, 464.
[140] J. Bonse, S. M. Wiggins, J. Solis, *J. Appl. Phys.* **2004**, *96*, 2352.
[141] S. Nakamura, T. Hibiya, *Int. J. Thermophys.* **1992**, *13*, 1061.
[142] E. L. Gurevich, *Appl. Surf. Sci.* **2016**, *374*, 56.
[143] J. Bonse, S. V. Kirner, J. Krüger, in *Handbook of Laser Micro- and Nano-Engineering* (Ed: K. Sugioka), Springer, Cham, Switzerland **2020**.
[144] J. Bonse, G. Mann, J. Krüger, M. Marcinkowski, M. Eberstein, *Thin Solid Films* **2013**, *542*, 420.
[145] C. Kunz, S. Engel, F. A. Müller, S. Gräf, *Nanomaterials* **2020**, *10*, 1187.
[146] J. Eichstädt, G. R. B. E. Römer, A. J. Huis in't Veld, *Appl. Surf. Sci.* **2013**, *264*, 79.
[147] M. Mezera, G. R. B. E. Römer, *Opt. Express* **2019**, *27*, 6012.
[148] L. Wang, X.-W. Cao, C. Lv, H. Xia, W.-J. Tian, Q.-D. Chen, S. Juodkazis, H.-B. Sun, *IEEE J. Quantum Electron.* **2018**, *54*, 9200207.

Jörn Bonse received a diploma degree in physics from the University of Hannover, and a doctoral degree from the Technical University of Berlin. He occupied research positions at the Laser Zentrum Hannover, the Max-Born-Institute in Berlin, the Spanish National Research Council in Madrid, and was appointed as a Senior Laser Application Specialist at Newport Spectra-Physics. Currently, he is a Senior Scientist at the German Federal Institute for Materials Research and Testing. His research interests include fundamentals and applications of laser-matter interaction, laser-induced periodic nanostructures, time-resolved optical techniques, laser processes in photovoltaics, and laser related safety aspects.

Stephan Gräf is a researcher and group leader at the Otto Schott Institute of Materials Research at the University in Jena. He received his PhD in 2010 from the University Jena in the field of laser welding with dynamically polarized CO_2 laser radiation. Within the past years his work mainly focused on the engineering of material surfaces with tailored functional properties. This includes the detailed study of laser-matter interaction with regard to different wavelengths and pulse durations as well as laser-assisted micro- and nanostructuring of surfaces, in particular the fabrication of laser-induced periodic surface structures using ultrashort pulsed laser radiation.